Geochemistry, Geophysics, Geosystems

RESEARCH ARTICLE
10.1029/2020GC009351

Key Points:

- Two-dimensional (2D) hydro-mechanical-chemical model couples rock deformation, porous fluid flow, and reactions for brucite-periclase (de)hydration reaction
- Rock heterogeneities affect reaction-front propagation and reaction-induced weakening and cause differences in fluid and rock pressure
- MATLAB code for numerical 2D hydro-mechanical-chemical model is provided

Supporting Information:

- Supplemental Material 1

Correspondence to:
S. M. Schmalholz,
stefan.schmalholz@unil.ch

Citation:
Schmalholz, S. M., Moulas, E., Plümper, O., Myasnikov, A. V., & Podladchikov, Y. Y. (2020). 2D hydro-mechanical-chemical modeling of (De)hydration reactions in deforming heterogeneous rock: The periclase-brucite model reaction. *Geochemistry, Geophysics, Geosystems*, *21*, 2020GC009351. https://doi.org/10.1029/2020GC009351

Received 7 AUG 2020
Accepted 3 OCT 2020

2D Hydro-Mechanical-Chemical Modeling of (De)hydration Reactions in Deforming Heterogeneous Rock: The Periclase-Brucite Model Reaction

Stefan M. Schmalholz[1], Evangelos Moulas[2], Oliver Plümper[3], Artem V. Myasnikov[4], and Yuri Y. Podladchikov[1,4]

[1]Institute of Earth Sciences, University of Lausanne, Lausanne, Switzerland, [2]Institut für Geowissenschaften, University of Mainz, Mainz, Germany, [3]Department of Earth Sciences, Utrecht University, Utrecht, The Netherlands, [4]Faculty of Mechanics and Mathematics, Moscow State University, Moscow, Russia

Abstract Deformation at tectonic plate boundaries involves coupling between rock deformation, fluid flow, and metamorphic reactions, but quantifying this coupling is still elusive. We present a new two-dimensional hydro-mechanical-chemical numerical model and investigate the coupling between heterogeneous rock deformation and metamorphic (de)hydration reactions. We consider linear viscous compressible and power-law viscous shear deformation. Fluid flow follows Darcy's law with a Kozeny-Carman type permeability. We consider a closed isothermal system and the reversible (de)hydration reaction: periclase and water yields brucite. Fluid pressure within a circular or elliptical inclusion is initially below the periclase-brucite reaction pressure and above in the surrounding. Inclusions exhibit a shear viscosity thousand times smaller than for the surrounding. For circular inclusions, solid deformation has a minor impact on the evolution of fluid pressure, porosity, and reaction front. For elliptical inclusions and far-field shortening, rock pressure inside the inclusion is higher compared to circular inclusions, and reaction-front propagation is faster. The reaction generates a large change in porosity (~0.1%–55%) and in solid density (~2,300–3,500 kg m^{-3}), and the reaction front exhibits steep gradients of fluid pressure and porosity. Reaction-front propagating increases the weak inclusion's surface and causes an effective, reaction-induced weakening of the heterogeneous rock. Weakening evolves nonlinear with progressive strain. Distributions of fluid and rock pressure as well as magnitudes and directions of fluid and solid velocities are significantly different. The models mimic basic features of shear zones and show the importance of coupling deformation and metamorphism. The applied MATLAB algorithm is provided.

Plain Language Summary Geodynamic processes at tectonic plate boundaries are complicated because rock deformation, fluid flow, and chemical reactions occur simultaneously. Investigating these coupled processes by direct observations is usually not possible, and investigating them with laboratory experiments is often not feasible. Alternatively, these coupled processes can be investigated with computer simulations. Here, we present a new two-dimensional hydro-mechanical-chemical computer model to investigate the coupling of these processes. We consider a simple and reversible (de)hydration reaction: periclase (magnesium oxide) and water yields brucite (magnesium hydroxide). The initial fluid pressure within a circular or elliptical inclusion is initially below the periclase-brucite reaction pressure, while in the surrounding it is above. Inclusions in the deforming rock are mechanically weaker than the surrounding. Models with elliptical inclusions generate higher rock pressure inside the inclusion compared to circular inclusions and show a faster reaction-front propagation. The propagating reaction-front causes an effective, reaction-induced weakening of the heterogeneous rock. Fluid and rock pressure as well as magnitudes and directions of fluid and solid velocities are significantly different. The models mimic basic features of shear zones and suggest a strong impact of heterogeneous rock deformation on (de)hydration reactions and associated rheological weakening. The applied MATLAB algorithm is provided.

1. Introduction

The deformation of lithospheric tectonic plates generates major rifts, strike-slip faults, and subduction zones and is, hence, a critical process for the evolution of our dynamic planet. Lithosphere deformation involves a

complex interplay between heat transfer, rock deformation, fluid flow, and metamorphic reactions. Notably, the interplay between heterogeneous rock deformation and metamorphic (de)hydration reactions, such as related to eclogitization, serpentinization, or decarbonation, may have a significant impact on, for example, the evolution of shear zones (e.g., Austrheim, 1987), faulting at slow-spreading ridges (e.g., Escartin et al., 1997), subduction interface processes (e.g., Guillot et al., 2015), or slip-weakening of faults due to decarbonation (e.g., Sulem & Famin, 2009). Hence, quantifying this interplay is essential for eventually understanding coupled plate tectonic processes. At present, however, such quantification remains elusive.

Many metamorphic reactions are intrinsically coupled to fluid flow since they involve the hydration or dehydration of rocks (e.g., Lindgren, 1912; Philpotts & Ague, 2009; Putnis, 2009; Yardley, 1989). Such metamorphic (de)hydration reactions occur when ambient pressure and temperature conditions change due to, for example, rock burial and subsequent exhumation (e.g., Philpotts & Ague, 2009; Yardley, 1989). Furthermore, stress and fluid-pressure variations due to tectonic, differential stresses can affect the region of thermodynamic equilibrium of hydrous/anhydrous phases (e.g., Jamtveit et al., 2019; Moulas et al., 2019; Wheeler, 2018). Fluid flow and associated (de)hydration reactions are essential for many first-order phenomena in plate boundary regions, which include, for example, fluid cycling through the lithosphere (e.g., John et al., 2011), the evolution of shear zones (e.g., Austrheim, 1987), slow-slip phenomena at subduction zones (e.g., Gomberg et al., 2010; Schwartz & Rokosky, 2007), intermediate-depth earthquakes (e.g., Brantut et al., 2017; Ferrand et al., 2017), reaction-induced rheological weakening of rocks (e.g., Jolivet et al., 2005; White & Knipe, 1978), or self-sustained densification of the lower crust (e.g., Malvoisin et al., 2020). These reactions may also be of industrial relevance, for example, for geological carbon sequestration (e.g., Kelemen & Matter, 2008) or volume changes during geothermal energy extraction.

Metamorphism and rock deformation often occur together (e.g., Hobbs & Ord, 2015; Yardley, 1989). From the view point of solid volume and mass changes, there are two end-member scenarios that couple (de) hydration reactions and rock deformation: (1) the volume of the considered solid-fluid system is constant during (de)hydration or (2) the pressure is constrained during (de)hydration while the volume is unconstrained. The first, constant volume, scenario requires mobility, input, and loss of the involved elements via dissolution and precipitation processes (e.g., Lindgren, 1912; Putnis, 2009). The considered fluid-rock system is open, but its mass exchange evolves in such a way that the rock volume is constant. For the particular case of an open system with constant volume, there is virtually no coupling between (de)hydration reactions and rock deformation, so that (de)hydration reactions can be investigated using pure hydro-chemical (HC) models assuming that velocities of the solid rock are zero (e.g., Plümper et al., 2017). In the second scenario, the volume is not constrained. Volume change occurs if the system is closed, and the elements are redistributing among the stable phases (e.g., Connolly, 1997; Malvoisin et al., 2015). For the case of a closed system with volume change, deformation of the porous solid coupled with (de)hydration reactions must be investigated using a hydro-mechanical-chemical (HMC) model (e.g., Poulet et al., 2012). Volume changes can be significant and may cause considerable deformation and differential stresses in the rock. These stresses can cause fracturing (e.g., Carmichael, 1987; Evans et al., 2020; Kelemen & Hirth, 2012; Plümper et al., 2012; Zheng et al., 2018), for example, during serpentinization (e.g., Kelemen & Hirth, 2012) or transition from anorthosite to eclogite (e.g., Jamtveit et al., 2000).

Furthermore, metamorphic reactions frequently occur during lithosphere deformation, which exhibits shear deformation significantly larger than the volumetric deformation. Deviatoric stresses drive shear deformation, and the mean stress in a deforming rock is, hence, not lithostatic (e.g., Schmalholz et al., 2014). Moreover, most deforming rock units are mechanically heterogeneous, due to, for example, their layered structure. These heterogeneities typically cause folding and necking in the deforming lithosphere across all geological scales (e.g., Schmalholz & Mancktelow, 2016). Furthermore, active shear zones are usually mechanically weaker than their wall rocks, so that rock units, including active shear zones, represent mechanically heterogeneous systems. Mechanical heterogeneities in deforming rocks cause stress and pressure variations within and around the heterogeneities (e.g., Moulas et al., 2014; Schmid & Podladchikov, 2003). Recent numerical models show that mechanical heterogeneities within subduction-related shear zones, and the associated stress variations, could explain slow slip events, that is, episodes of aseismic slip commonly associated with tectonic tremor, which are observed along subduction interfaces (e.g., Beall et al., 2019a, 2019b; Webber et al., 2018). These purely mechanical models do not yet consider fluid flow and

reactions. Eventually elaborating such mechanically heterogeneous shear zone models by including fluid flow and reactions is, hence, important for ultimately understanding subduction interface processes and for unraveling the interplay between lithosphere deformation and metamorphic reactions.

A method to quantify the interplay between lithosphere deformation, fluid flow, and metamorphic reactions is mathematical modeling. A particular challenge for such models is the significantly different temporal and spatial scales of fluid flow and viscous flow of the lithospheric rocks (e.g., Quinquis & Buiter, 2014). Therefore, many numerical models focusing on lithosphere deformation employ significantly simplified models to quantify fluid flow and/or reactions (e.g., Quinquis & Buiter, 2014). For example, in some earlier models, the magnitude and direction of fluid velocity are prescribed to a constant value (e.g., T. V. Gerya et al., 2008). In other models, the fluid velocity is described by a Darcy-type law, but it is assumed that the fluid pressure is equal to the rock pressure (e.g., Yang & Faccenda, 2020). In contrast to such lithospheric-scale models, two-phase models can calculate both solid deformation and fluid flow, based on a self-consistent system of governing equations (e.g., Biot, 1941; Coussy, 2004; Evans et al., 2018; Yarushina & Podladchikov, 2015). However, many of these models are currently still assuming that solid deformation is negligible and set the solid velocities to zero (e.g., Beinlich et al., 2020; Plümper et al., 2017). Other models focus on homogeneous deformation and ignore shear deformation or mechanical heterogeneities (e.g., Brantut et al., 2011; Malvoisin et al., 2015).

Here, we aim to take a further step toward quantifying the interplay between heterogeneous rock deformation, fluid flow, and metamorphic reactions. We study the impact of volumetric and shear deformation on fluid flow and (de)hydration reactions in a mechanically heterogeneous, poroviscous medium. Our two-dimensional (2D) mathematical model for HMC two-phase processes extends the model of Malvoisin et al. (2015). The mechanical part of our HMC model can calculate stress and pressure variations around mechanically weak, or strong, inclusions in a compressible power-law viscous medium under far-field pure-shear shortening. We study the deformation of a medium with weak elliptical inclusions because such a model captures the first-order stress and deformation features of weak lithospheric shear zones (Moulas et al., 2014). The HC part of the model can calculate the evolution of fluid pressure, porosity, and solid as well as fluid densities including (de)hydration reactions. Although our HMC model is generally applicable, for transparency and clarity, we apply the model here to a simple brucite ($Mg(OH)_2$) − periclase (MgO) − water (H_2O) system (Figure 1). We also chose the brucite-periclase (de)hydration reaction because it involves considerable volume and porosity changes (e.g., Carmichael, 1987; Zheng et al., 2018) and is, hence, a good test for the numerical robustness of our HMC model. For simplicity, we assume a constant temperature and a constant system composition (closed system), and we assume that solid and fluid densities are only a function of the fluid pressure.

The aims of our study are as follows: (1) to present a self-consistent system of equations to quantify (de) hydration reactions and fluid flow in mechanically heterogeneous and deforming poroviscous rock, (2) to present a numerical pseudo-transient finite-difference algorithm to solve the system of equations, (3) to quantify the impact of volumetric and shear deformation on the brucite-periclase (de)hydration reaction and the evolving reaction front, (4) to quantify differences between fluid and rock pressure, and between fluid and solid velocities, and (5) to quantify the reaction-induced rheological weakening of the modeled heterogeneous rock.

2. Mathematical Model

2.1. Porous Medium Densities for the Brucite, Periclase, and Water System

We consider a porous medium, with porosity ϕ, which consists of a solid phase with density ρ_s and a pore fluid with density ρ_f so that the total density of the porous medium is

$$\rho_T = \rho_f \phi + \rho_s \left(1 - \phi\right). \tag{1}$$

We assume that the solid phase consists of two components: (1) a nonvolatile component that remains in the solid and (2) a volatile component that is liberated during dehydration. For the considered brucite-periclase

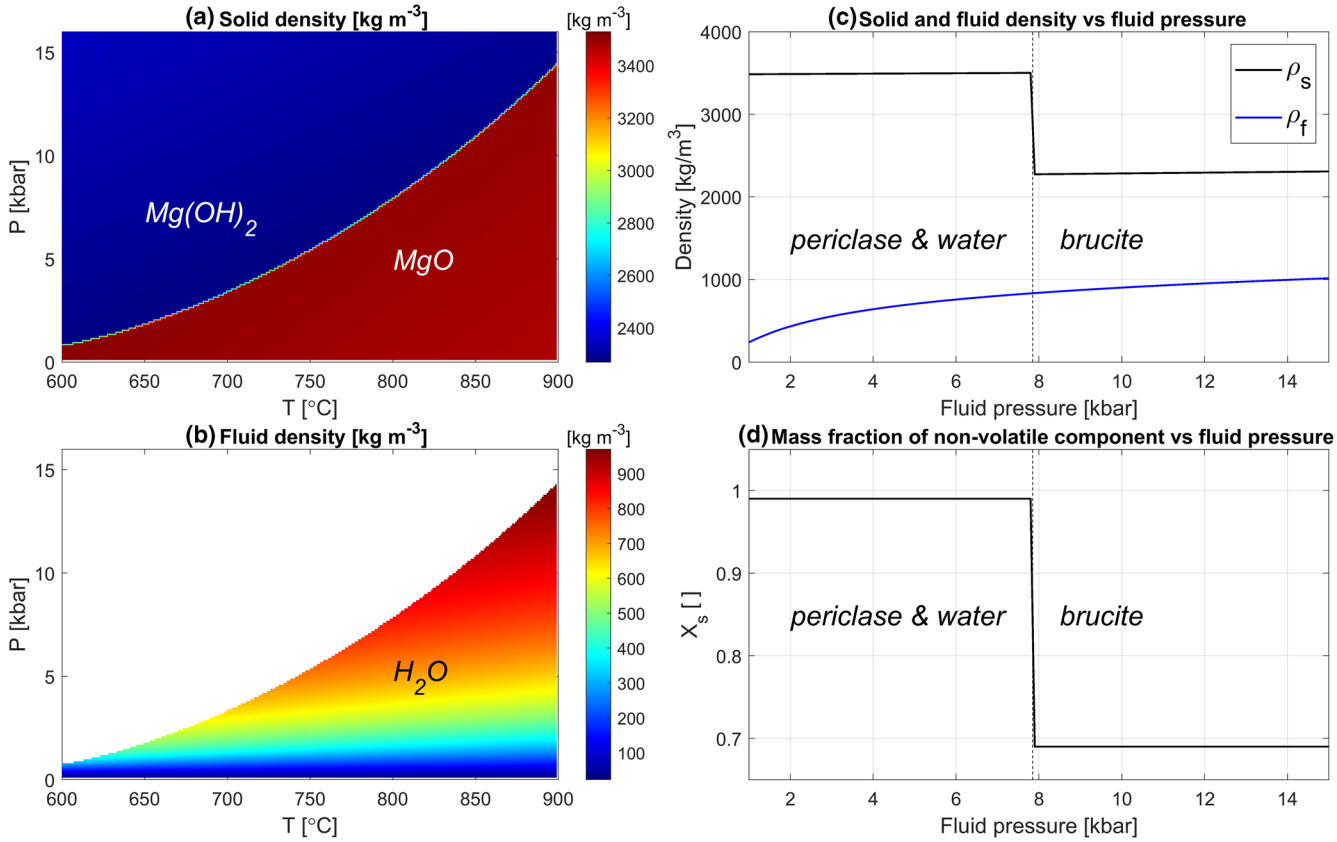

Figure 1. (a) Solid and (b) fluid density fields in pressure, P, and temperature, T, space. (c) and (d) Corresponding profiles of solid and fluid densities and mass fraction of MgO as a function of fluid pressure at 800°C. These three profiles are used in the numerical algorithm as precalculated data.

system, the nonvolatile component is MgO, and the volatile component is H_2O. To quantify the nonvolatile component of MgO in the solid phase, we use its mass (in kg) fraction, X_s. Periclase has a molar mass of 0.0403 kg/mol, water of 0.0180 kg/mol and brucite of 0.0583 kg/mol. Therefore, we set $X_s = 1$ for periclase and $X_s = 0.69$ for brucite. Furthermore, we define the relative density of the solid component in the solid phase as

$$\rho_X = \rho_s X_s \tag{2}$$

2.2. HC Model

The conservation of total mass is described by

$$\frac{\partial \rho_T}{\partial t} + \nabla\left[\rho_f \phi \mathbf{v}^f + \rho_s (1-\phi)\mathbf{v}^s\right] = 0, \tag{3}$$

where t is time, ∇ is the divergence operator, and $\mathbf{v}^f$ and $\mathbf{v}^s$ are vectors of the fluid and solid (barycentric) velocities, respectively. For vector and tensor quantities, we use indices f and s as superscripts because vector and tensor components will have additional subscripts indicating the spatial direction, and scalar quantities can be easier distinguished from vector and tensor quantities. We modify Equation 3 by subtracting and adding $\mathbf{v}^s$ to $\mathbf{v}^f$, yielding

$$\frac{\partial \rho_T}{\partial t} + \nabla\left[\rho_f \phi\left(\mathbf{v}^f - \mathbf{v}^s + \mathbf{v}^s\right) + \rho_s (1-\phi)\mathbf{v}^s\right] = 0. \tag{4}$$

Then, we re-group the velocity vectors with the total density, ρ_T, to yield

$$\frac{\partial \rho_T}{\partial t} + \nabla\left[\rho_f \phi\left(\mathbf{v}^f - \mathbf{v}^s\right)\right] + \nabla\left(\rho_T \mathbf{v}^s\right) = 0. \tag{5}$$

Now, the relative velocity of the fluid to the solid, $\mathbf{v}^f - \mathbf{v}^s$, in Equation 5 can be expressed by Darcy's law in the absence of gravity

$$\phi\left(\mathbf{v}^f - \mathbf{v}^s\right) = -\frac{k\phi^3}{\eta_f}\nabla p_f. \tag{6}$$

where k is the permeability coefficient in a Kozeny-Carman-type permeability expression, η_f is the fluid viscosity, and p_f is the fluid pressure. Similar to total mass, the conservation of the total nonvolatile component (MgO) is described by

$$\frac{\partial}{\partial t}\left[\rho_X\left(1-\phi\right)\right] + \nabla\left[\rho_X\left(1-\phi\right)\mathbf{v}^s\right] = 0. \tag{7}$$

There is no fluid velocity in this conservation equation because we assume that the dissolution of MgO in the fluid is negligible.

We assume a constant temperature and a closed system with constant system composition so that we have equal molar amounts of H_2O and MgO. Our system has a constant composition as a whole, but its composition can vary locally because of local mass exchange (e.g., reaction and/or diffusion). We approximate ρ_s, ρ_f, and X_s as a function of p_f, which can be expressed as

$$\begin{aligned} \rho_f &= \rho_f\left(p_f\right) \\ \rho_s &= \rho_s\left(p_f\right) \\ X_s &= X_s\left(p_f\right). \end{aligned} \tag{8}$$

The values of ρ_s, ρ_f, and X_s for a range of values of p_f are calculated by Gibbs free-energy minimization (e.g., Connolly, 2005; Figure 1), using the thermodynamic data set of Holland and Powell (1998).

2.3. Mechanical Model

We consider a 2D viscous material, which represents the solid part of the poroviscous medium. We employ a power-law viscous flow law, which is typically applied to model dislocation creep (e.g., Gerya, 2019). The relationship between the deviatoric stress tensor components, $\tau_{ij} = \sigma_{ij} + p\delta_{ij}$ (where σ_{ij} are the components of the total stress tensor, p is total pressure and δ_{ij} is the Kronecker delta) and solid velocity gradients, or deviatoric strain rate tensor components D_{ij}, is (e.g., Fletcher, 1974; Schmalholz & Schmid, 2012)

$$\tau_{ij} = 2\eta^s\left(\frac{\tau_{II}}{\tau_{ref}}\right)^{1-n} D_{ij}, \tag{9}$$

where subscripts i and j are either 1 (representing the horizontal x-direction) or 2 (representing the vertical y-direction), η^s is the solid shear viscosity, τ_{II} is the square root of the second invariant of the deviatoric stress tensor, $\tau_{II} = \sqrt{\tau_{xx}^2 + \tau_{xy}^2}$, τ_{ref} is a reference stress, n is the stress exponent, and $D_{ij} = \left(\partial v_i^s / \partial x_j + \partial v_j^s / \partial x_i\right)/2 - \delta_{ij}\left(\partial v_i^s / \partial x_i\right)/3$. For $n = 1$, the material is linear viscous, for example mimicking diffusion creep, having a constant viscosity η^s. For simplicity, we also consider a viscous volumetric deformation for which the divergence of the solid velocity field is related to the difference between total pressure, p, and fluid pressure, p_f (e.g., Yarushina & Podladchikov, 2015)

Table 1
Model Variables and Parameters

Symbol	Name/definition	Units
p_f	Fluid pressure	Pa
φ	Porosity	-
ρ_s	Solid density	$kg{\cdot}m^{-3}$
ρ_f	Fluid density	$kg{\cdot}m^{-3}$
X_s	Mass fraction MgO	-
p	Total pressure	Pa
v_x^s, v_y^s	Solid velocities	$m{\cdot}s^{-1}$
$\left\|\mathbf{v}^s\right\|$	$=\sqrt{\left(v_x^s\right)^2+\left(v_y^s\right)^2}$	$m{\cdot}s^{-1}$
v_x^f, v_y^f	Fluid velocities	$m{\cdot}s^{-1}$
$\left\|\mathbf{v}^f\right\|$	$=\sqrt{\left(v_x^f\right)^2+\left(v_y^f\right)^2}$	$m{\cdot}s^{-1}$
τ_{xx}, τ_{yy}, τ_{xy}	Deviatoric stresses	Pa
τ_{II}	$=\sqrt{\tau_{xx}^2+\tau_{xy}^2}$	Pa
τ_{ref}	Reference stress	Pa
k	Permeability	m^2
η_f	Fluid viscosity	Pa·s
η^s	Shear viscosity solid	Pa·s
λ	Bulk viscosity solid	Pa·s
n	Stress exponent	-
β_{eff}	Effective compressibility	Pa
p_{ini}	Initial ambient pressure	Pa
$\bar{D}_{xx}$	Far-field shortening rate	s^{-1}
r	Inclusion radius	m
w	Model width	m

$$\nabla \mathbf{v}^s = -\frac{p - p_f}{(1-\phi)\lambda}, \tag{10}$$

where λ is the bulk viscosity. The applied force balance equations without inertial forces and gravity are

$$\nabla \sigma_{ij} = 0. \tag{11}$$

2.4. Governing System of Equations

The above equations represent a system of 11 equations for 11 unknowns, which are p_f, ϕ, ρ_s, ρ_f, X_s, p, v_x^s, v_y^s, τ_{xx}, τ_{yy}, and τ_{xy}, assuming that the deviatoric stress tensor is symmetric, $\tau_{xy} = \tau_{yx}$. The three deviatoric stress tensor components are calculated using the three flow laws (Equation 9). The solid pressure is determined from the bulk-flow law, Equation 10. The solid and fluid densities and the mass fraction are calculated by the three precomputed thermodynamic data tables (Equation 8 and Figures 1c and 1d). Equation 5 is used to determine the fluid pressure, p_f, Equation 7 to determine the porosity, ϕ, and the two force balance Equation 11 to determine the two solid velocities, v_x^s and v_y^s. To determine p_f, ϕ, v_x^s, and v_y^s, we use an iterative numerical method, here referred to as pseudo-transient (PT) method (e.g., Chorin, 1968; Duretz et al., 2019; Räss et al., 2019). We apply the PT method because (1) it is a suitable method to solve fully coupled, nonlinear problems due to its iterative nature, (2) it is fully matrix free and easy to program, and (3) the developed 2D model is easily extendable for 3D. To apply the PT method, we add a pseudo time derivative of the unknown variables p_f, ϕ, v_x^s, and v_y^s to the corresponding equations, which we use to determine these variables. The PT equations are

$$\begin{aligned}
\frac{\partial^{PT} p_f}{\partial t_{pf}^{PT}} &= -\frac{\partial \rho_T}{\partial t} + \nabla\left[\rho_f \frac{k\phi^3}{\eta_f}\nabla p_f\right] - \nabla\left(\rho_T v^s\right) \\
\frac{\partial^{PT} \phi}{\partial t_{\phi}^{PT}} &= \frac{\partial}{\partial t}\left[\rho_X(1-\phi)\right] + \nabla\left[\rho_X(1-\phi)v^s\right] \\
\frac{\partial^{PT} v_i^s}{\partial t_v^{PT}} &= \nabla \sigma_{ij}
\end{aligned} \tag{12}$$

When the PT time derivatives of the left-hand sides of the Equation 12 are zero, then the corresponding steady-state equations are solved. The closed system of governing equations is given by Equations 8–10 and 12. Model variables and parameters are given in Table 1.

2.5. Model Configuration

We present the model configuration before presenting the numerical method because some of the numerical parameters, such as the numerical time step, depend on the model configuration (Figure 2). It is essential to apply physically consistent initial conditions. Hence, we first assume ambient conditions for which

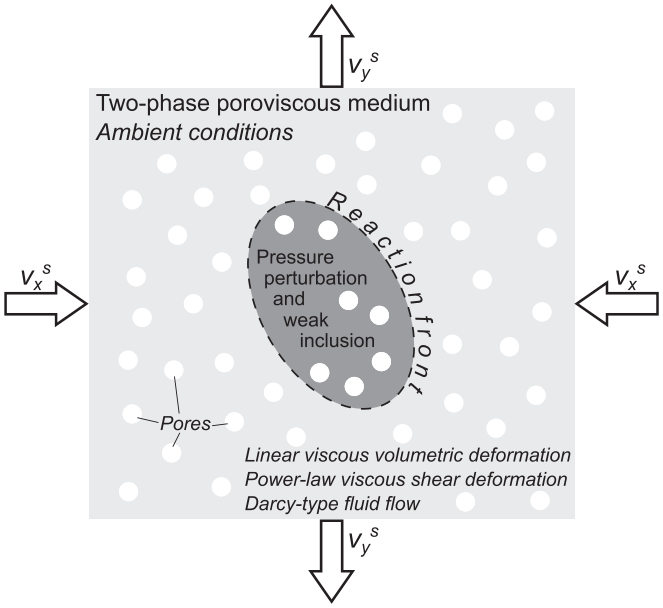

Figure 2. Sketch of the modeled scenario and the model configuration (see text for details).

the unknown parameters are constant in the 2D model domain. We then apply an initial perturbation for p_f in a circular, or elliptical, region, representing an inclusion, in the center of the model domain (Figure 3). We consider different aspect ratios and orientations for the elliptical inclusions. The origin of the coordinate system is always at the center of the inclusions with positive coordinates indicating toward the right side and upwards. The initial perturbation either increases or decreases the ambient value of p_f. We consider two initial configurations: (1) ambient conditions for which periclase and water are stable with a positive fluid-pressure perturbation generating locally higher fluid pressures inside the inclusion for which brucite is stable and (2) ambient conditions for which brucite is stable and a negative pressure perturbation for which locally periclase and water are stable. The initial porosity field, ϕ_0, must be consistent with the applied initial fluid pressure field including a pressure perturbation. The initial porosity is

$$\phi^0 = 1 - \frac{\rho_X^{amb}\left(1-\phi^{amb}\right)}{\rho_X^0}, \tag{13}$$

where ρ_X^{amb} is the corresponding density for the applied ambient fluid pressure, ϕ^{amb} is the initially ambient porosity, and ρ_X^0 is the initial density field for the initial fluid-pressure field including the perturbation. Equation 13 shows that ϕ_0 cannot be constant initially if a fluid pressure perturbation is applied because ρ_X^0 varies according to the applied fluid pressure perturbation. Equation 13 is derived from Equation 7, assuming zero solid velocities. To guarantee that ϕ_0 is initially everywhere positive requires, according to Equation 13, that $\phi^{amb} > 1 - \rho_X^0 / \rho_X^{amb}$. Boundary conditions for p_f and ϕ are of Dirichlet type, and boundary values are fixed to the initial ambient values.

We also show simulations for a configuration with inclusions, which have a smaller shear viscosity being 1,000 times smaller than the one of the surrounding (Figures 6–10). Furthermore, we show simulations for far-field pure-shear shortening boundary conditions, with horizontal shortening and vertical extension, so that the divergence of the applied boundary velocity field is zero (Figures 6–10). We assume a constant temperature of 800°C so that there is a sufficient range of fluid pressures for which periclase is stable (Figure 1a). The exact temperature value is not essential for our isothermal study because the variation of the solid and fluid densities with varying fluid pressure is similar for different temperatures (Figures 1a and 1b).

2.6. Numerical Algorithm and Dimensionless Parameters

All derivatives are approximated with discrete difference ratios following the standard procedure of staggered finite difference (FD) methods (e.g., Gerya, 2019). The numerical algorithm consists of a standard time loop with an internal PT iteration loop. During this PT iteration loop, the PT time derivatives in the discretized Equation 12 approach zero. In practice, we iterate until the PT time derivative becomes smaller than a specified numerical tolerance error. Approximating the time derivatives with the FD method generally requires four numerical time steps, which are the physical time step, Δt, controlling time evolution, the PT time step to solve for p_f, Δt_{pf}^{PT}, the PT time step for ϕ, Δt_ϕ^{PT}, and the PT time step for v_x^s and v_y^s, Δt_v^{PT}. The choice of the numerical time steps is crucial for a stable convergence of the PT iterative solution, but the time steps do not affect the result after convergence. For the presented simulations, we employed the following numerical time steps:

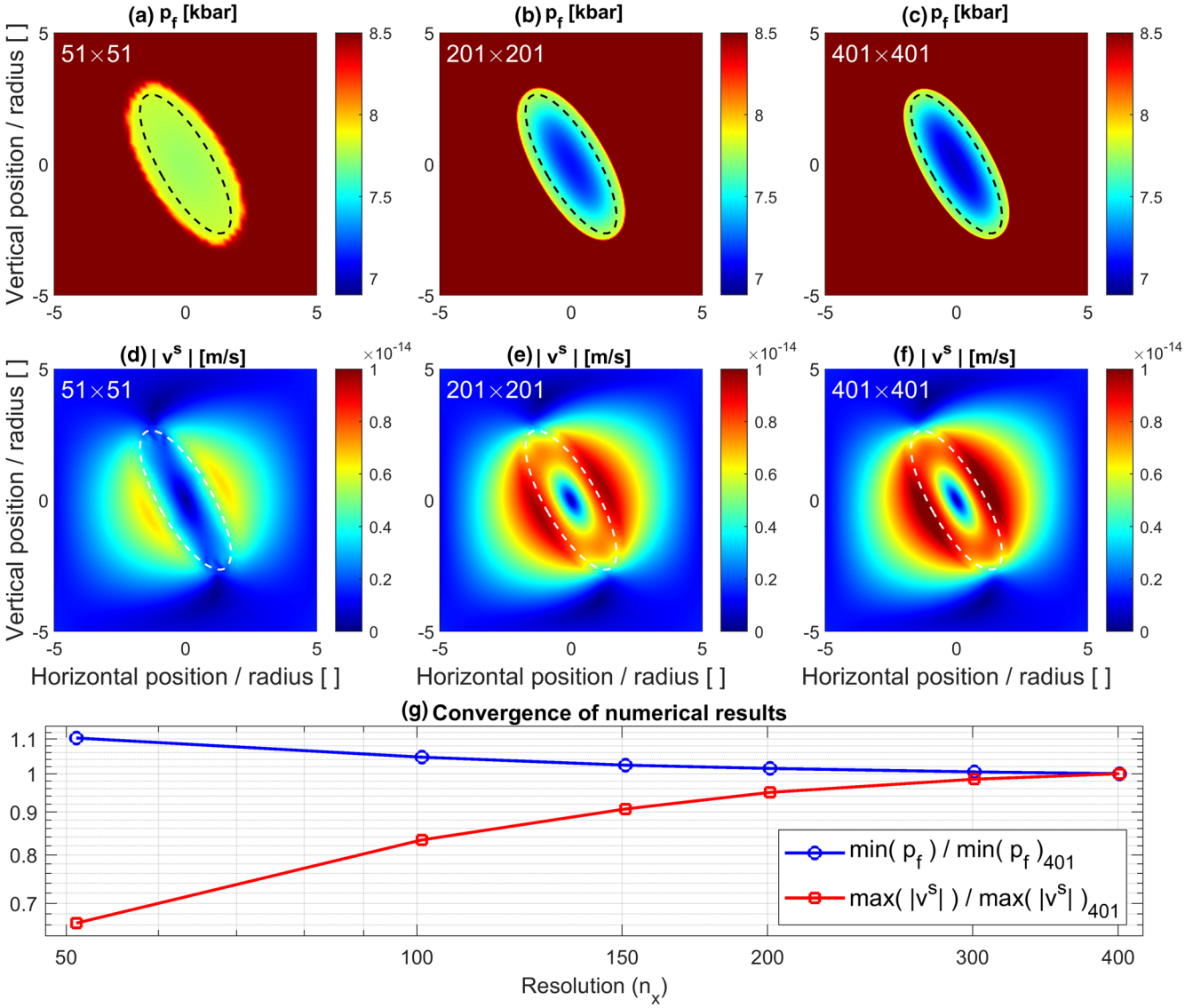

Figure 3. Numerical convergence test for a model with a weak and oblique elliptical inclusion under far-field horizontal pure-shear shortening. The model is described and discussed in detail later in Section 3 and more results of the model are displayed in Figures 9 and 10. The presented results of the convergence test correspond to a model time of 3.3 h. (a–c) Color plot of p_f for three different numerical resolutions (white numbers inside panel). (d–f) Color plot of $\left|\mathbf{v}^s\right| = \sqrt{\left(v_x^s\right)^2 + \left(v_y^s\right)^2}$ for three different numerical resolutions (white numbers inside panel). (g) Variation of the minimum value of p_f and the maximal value of $\left|\mathbf{v}^s\right|$ with increasing resolution. The horizontal axis shows the resolution in the horizontal *x*-direction, and the vertical axis shows the corresponding quantities for p_f and $\left|\mathbf{v}^s\right|$ divided by the corresponding value for the maximal resolution of 401 grid points. The plot shows that the respective values vary less and less with increasing resolution indicating an asymptotic convergence of the numerical result toward a specific magnitude.

$$\begin{aligned}
\Delta t &= 2\frac{r^2\eta_f}{k\,\beta_{\text{eff}}} \\
\Delta t_{pf}^{PT} &= \frac{1}{16}\frac{\max\left(\Delta x,\Delta y\right)^2}{\max\left(\dfrac{k\,\phi^3}{\beta_{\text{eff}}}\right)} \\
\Delta t_{\phi}^{PT} &= \Delta t \\
\Delta t_{v}^{PT} &= \frac{1}{16}\frac{\max\left(\Delta x,\Delta y\right)^2}{\max\left(\eta^s\right)},
\end{aligned} \tag{14}$$

where $\beta_{\text{eff}} = 0.01 / p_{\text{ini}}$, r is the inclusion radius (the small radius in case of an elliptical inclusion), Δx and Δy are horizontal and vertical grid spacing, respectively, and p_{ini} is the initial value of the ambient fluid pressure. There are many possibilities to scale and/or nondimensionalize the model parameters inside the numerical algorithm. We programmed the numerical algorithm in such a way that the specific magnitudes of individual parameters, such as shear viscosity, are not significant and that the characteristic physical behavior of the system is controlled by dimensionless parameters. This scaling provided the most stable convergence during the PT iterations. The dimensionless parameters and numerical examples applied in the simulations are

$$\begin{aligned}
\Gamma_1 &= \frac{w}{r},\ \text{e.g.,}\Gamma_1 = \frac{10^{-1}\text{m}}{10^{-2}\text{m}} = 10 \\
\Gamma_2 &= \frac{k}{\eta_f}\frac{\eta^s}{r^2},\ \text{e.g.,}\Gamma_2 = \frac{10^{-19}\text{m}^2}{10^{-3}\text{Pas}}\frac{10^{20}\text{Pas}}{\left(10^{-2}\text{m}\right)^2} = 10^8 \\
\Gamma_3 &= \frac{\lambda}{\eta^s},\ \text{e.g.,}\Gamma_3 = \frac{10^{20}\text{Pas}}{10^{20}\text{Pas}} = 1 \\
\Gamma_4 &= \frac{\bar{D}_{xx}\eta^s}{p_{ini}},\ \text{e.g.,}\Gamma_4 = \frac{2\times10^{-14}s^{-1}10^{20}\text{Pas}}{8.5\times10^8\text{Pa}} = 0.0024 \\
\Gamma_5 &= \frac{\tau_{ref}}{p_{ini}},\ \text{e.g.,}\Gamma_5 = \frac{2.5\times10^7\text{Pa}}{8.5\times10^8\text{Pa}} = 0.024,
\end{aligned} \tag{15}$$

where w is the model width and $\bar{D}_{xx}$ is the applied far-field horizontal pure-shear shortening rate. We model purely mechanical, M, (fluid velocity is zero, no reactions), purely HC, (solid velocity is zero), and fully coupled HMC, systems. Parameter Γ_1 applies to all systems, parameter Γ_2 to HC systems and parameters Γ_3, Γ_4, and Γ_5 to HMC systems, where Γ_4 controls the far-field deformation via $\bar{D}_{xx}$ and Γ_5 only applies for power-law viscous deformation, $n > 1$.

The shear viscosity of the inclusion can be different from the one of the surrounding medium. The initial inclusion boundary represents the reaction boundary between brucite and periclase. This boundary will move during the simulations with progressive fluid pressure diffusion. Hence, also the boundary between regions of high porosity (periclase and water region) and low porosity will move. The boundary between brucite and periclase is controlled by a considerable change in porosity. Therefore, we define the brucite-periclase boundary by the average porosity between the brucite and periclase-water region. The brucite-periclase reaction boundary evolves, together with the evolving porosity field. At each time step, the shear viscosity distribution is adjusted in order to coincide with the evolving reaction boundary. Therefore, the size and geometry of the mechanically weaker inclusion are changing as time progresses.

To show in this section also a representative numerical convergence test of the algorithm, we performed a HMC simulation, which is described and discussed in detail below (Figures 9 and 10), for different numerical resolutions (Figure 3). We run simulations with resolutions of 51 × 51, 101 × 101, 151 × 151, 201 × 201, 301 × 301, and 401 × 401 grid points until a time corresponding to 3.3 h. The distribution of p_f (Figures 3a–3c) and $\left|\mathbf{v}^s\right| = \sqrt{\left(v_x^s\right)^2 + \left(v_y^s\right)^2}$ (Figures 3d–3f) does not show numerical oscillations around the dehydration front, although the numerically calculated fields of p_f and $\left|\mathbf{v}^s\right|$ have not been smoothed during

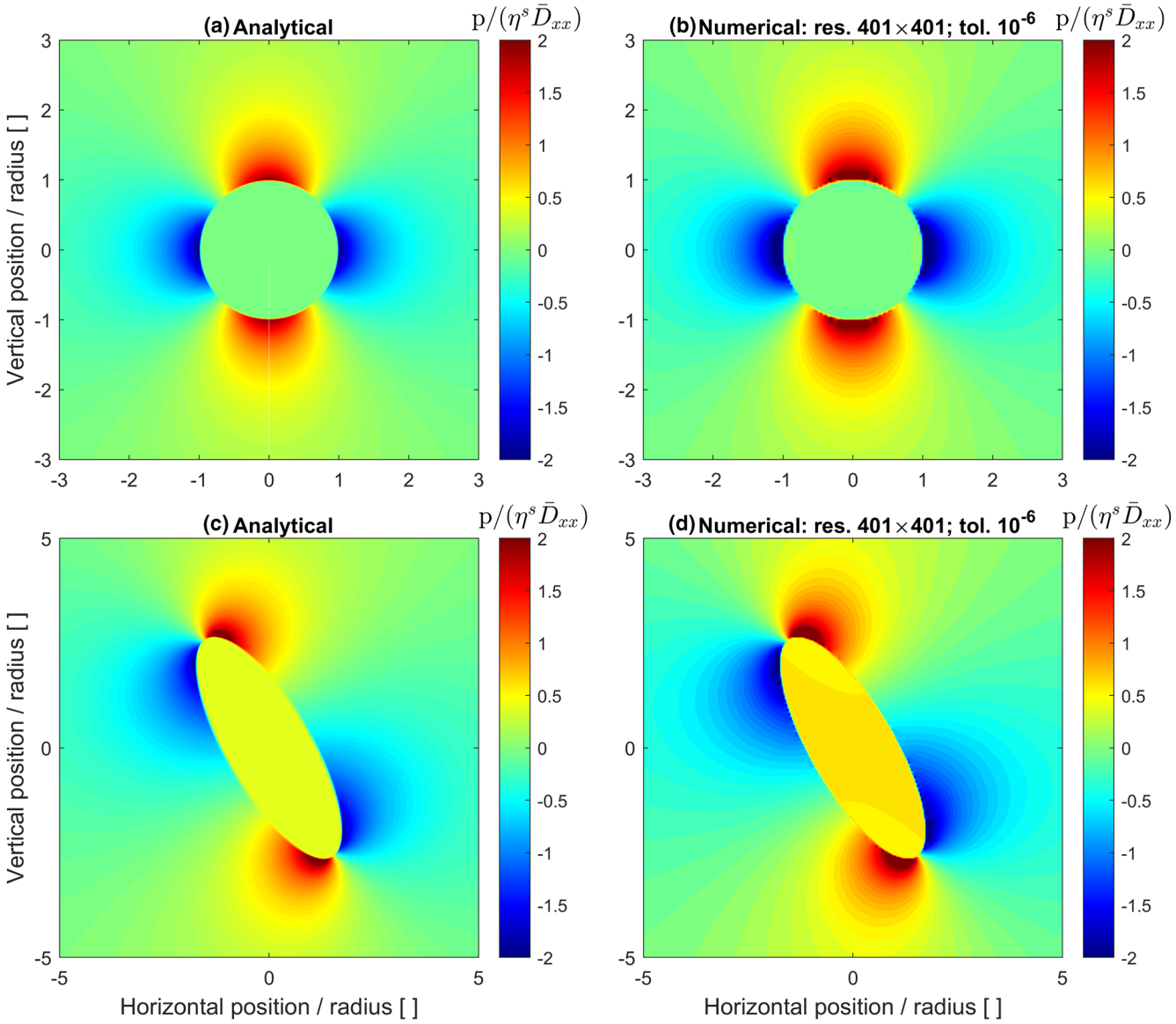

Figure 4. Numerical results of the mechanical model without fluid flow and reaction. (a) and (c) Total pressure field from analytical solutions of Moulas et al. (2014) for a weak circular and weak oblique elliptical inclusion under horizontal shortening. (b) and (d) Corresponding numerical results. The numerical model reproduces the characteristic pressure distribution and magnitudes.

the simulations. The minimal value of p_f at the end of each simulation varies for the different numerical resolutions, but it varies less and less with increasing resolution indicating the numerical convergence (Figure 3g). Similarly, the maximal value of $|\mathbf{v}^s|$ at the end of each simulation varies less and less with increasing resolution (Figure 3g). The convergence test indicates that the pseudo-transient finite difference (PTFD) algorithm is robust and suitable to numerically simulate the coupling of heterogeneous rock deformation, porous fluid flow, and metamorphic reactions.

We programmed the numerical algorithm in MATLAB. We provide the entire algorithm for the most complex HMC model configuration (Figure 9), which is available online (https://zenodo.org/badge/latestdoi/284908588).

3. Results

We present first results of a mechanical (M) model to test the applicability of the PTFD method considering viscous compressible flow for the calculation of pressure variations around weak inclusions under far-field shortening (e.g., Moulas et al., 2014; Schmid & Podladchikov, 2003). To test our system of equations and algorithm further, we show results of a HC model, which reproduce the overall results for nonlinear diffusion of fluid pressure perturbations (Malvoisin et al., 2015). Finally, we present fully coupled HMC models to test the impact of far-field deformation and mechanical heterogeneities on fluid flow and reaction-front evolution.

3.1. Heterogeneous Mechanical Model

A weak circular inclusion is embedded in a linear viscous medium under horizontal pure-shear shortening (Figures 2, 4a, and 4b). The applied dimensionless parameters are $\Gamma_1 = 14$, $\Gamma_3 = 1$, and $\Gamma_4 = 0.0024$. We also consider an elliptical inclusion (Figures 4c and 4d). The aspect ratio of the ellipse is three, and the long axis is tilted 30° to the vertical direction. The applied dimensionless parameters are $\Gamma_1 = 14$ (where the radius corresponds to the short axis of the ellipse), $\Gamma_3 = 1$ and $\Gamma_4 = 0.0024$. Inside the circular and elliptical inclusion, η^s is a factor 1,000 smaller than in the surrounding medium. We calculate the distributions of p and compare them with the corresponding analytical solutions from Moulas et al. (2014). The results show that the applied PTFD algorithm with a staggered Eulerian grid can calculate the characteristic pressure variations around the weak inclusions under far-field shortening (Figure 4). The numerical and analytical solutions are not fully comparable because (1) the analytical solution considers incompressible deformation while the numerical algorithm considers viscous volumetric deformation and (2) the analytical solution applies to an infinite domain while in the numerical model the pure-shear boundary conditions are applied at the boundaries of the finite model domain. However, the numerical and analytical solutions show similar magnitudes and distribution of p.

3.2. HC Model

We consider a porous medium without solid deformation and set the solid velocities to zero. Initially, the ambient fluid pressure and porosity are perturbed within a circular domain (Figure 5). This domain has the same viscosity as the surrounding and the model is mechanically homogeneous. We apply the parameters $\Gamma_1 = 10$ and $\Gamma_2 = 10^8$.

First, we apply an initially higher fluid pressure in the circular region so that initially brucite is stable inside the inclusion and periclase is stable outside the inclusion. The initial ambient value of $p_f = p_{\text{ini}} = 6.5$ kbar and in the inclusion $p_f = 8.45$ kbar. The ambient initial $\phi = 0.55$ and in the inclusion $\phi = 0.007$. We chose this porosity distribution to test the algorithm in the limit of low porosity. Figure 5 shows horizontal profiles of p_f and ϕ through the left model half, centered vertically, so that the right end of the displayed horizontal profiles is at the center of the inclusion. The model configuration is similar to models of Malvoisin et al. (2015) for reactions with positive Clapeyron slope (their Figures 10e and 10f). With progressive time, the initially step-like perturbation of p_f is diffusing while the profile of ϕ maintains a step-like shape representing the motion of a dehydration front, indicating the release of water from brucite (Figures 5a and 5b). Once values of p_f drop below 7.85 kbar, which is the value that defines the reaction from brucite to periclase, no brucite is present anymore in the model, which is indicated by constant $\phi = 0.55$.

Second, we apply an initially smaller fluid pressure in the circular region so that initially periclase is stable inside the inclusion and brucite is stable outside the inclusion. At first, the ambient value of $p_f = 8.5$ kbar and inside the inclusion $p_f = 6.8$ kbar. The ambient initial $\phi = 0.001$ and in the inclusion $\phi = 0.55$, again to test the algorithm in the limit of low porosity. This configuration corresponds to models shown in Figures 10g and 10h of Malvoisin et al. (2015). With progressive time, the step-like perturbation of p_f is diffusing, but the profile of p_f maintains a steep gradient for fluid pressure > 7.85 kbar, which is the pressure at the reaction from brucite to periclase (Figures 1c and 1d). The profile of ϕ also maintains a steep gradient representing the motion of a dehydration front, which moves outward toward the brucite region (Figures 5c and 5d).

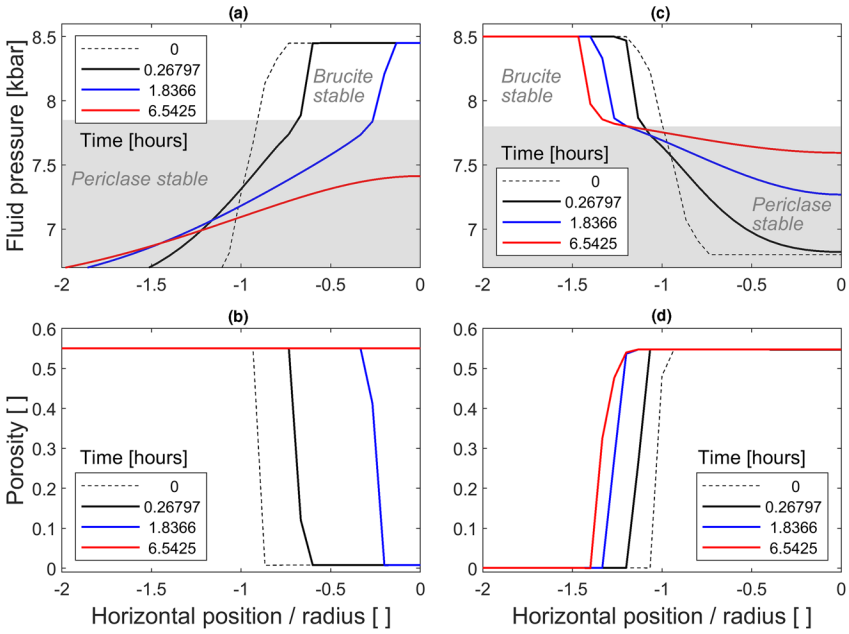

Figure 5. Numerical results of the hydro-chemical model, for which solid velocities are set to zero. The plots show horizontal profiles of p_f and ϕ through the left model half, centered vertically, so that the right end of the displayed profile is at the center of the inclusion. Evolution of fluid pressure for positive (a) and negative (c) initial pressure perturbations in circular inclusion. The gray-shaded region indicates the fluid pressure range for which periclase is stable. Corresponding evolution of porosity (b and d). Numbers in legend indicate modeled time in hours.

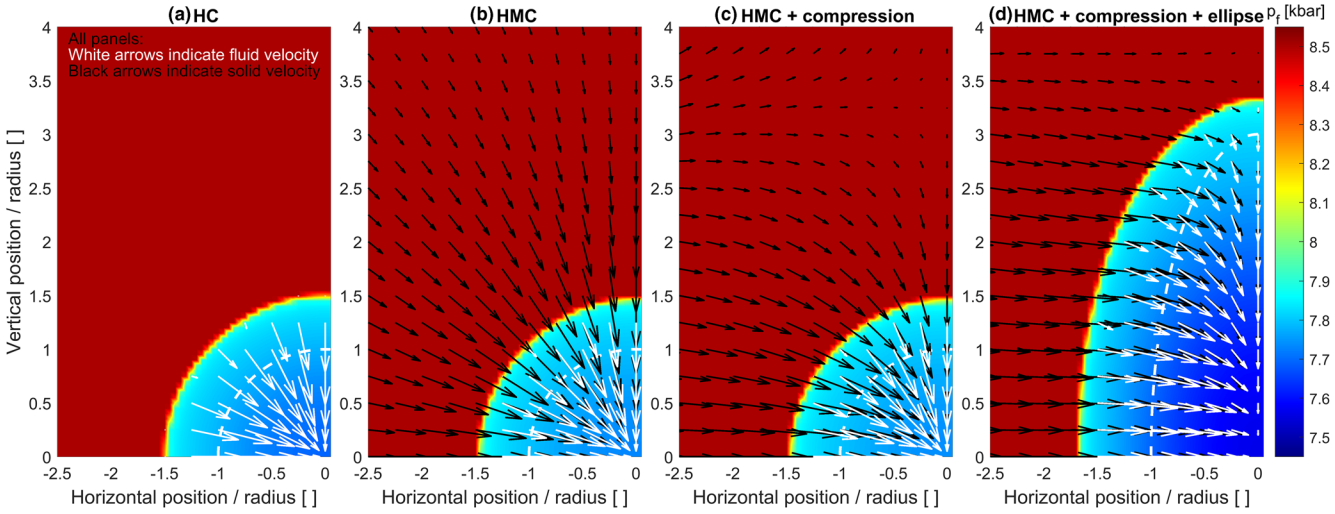

Figure 6. Color plot indicating the distribution of fluid pressure, p_f, and arrows indicating fluid (white arrows) and solid (black arrows) velocities for four simulations at a model time of 39.2 h. The circular and elliptical inclusion exhibited initially a smaller fluid pressure than the surrounding and the shear viscosity is a factor 1,000 smaller than the one of the surrounding (see text for details). (a) Hydro-chemical (HC) model (solid velocities are zero) with circular inclusion and no far-field shortening. (b) Hydro-mechanical-chemical (HMC) model with circular inclusion and no far-field shortening. (c) HMC model with circular inclusion and with far-field shortening. (d) HMC model with elliptical inclusion of initial aspect ratio of three and with far-field shortening. The white dashed line indicates the initial size of the perturbation. Solid and fluid velocity arrows are calculated and plotted at the same position.

For the case of a brucite-inclusion with higher fluid pressure (Figures 5a and 5b), the initially steep fluid pressure gradients decrease during the fluid pressure diffusion. At a certain time, the fluid pressure in the inclusion decreases below the reaction pressure of ca. 7.85 kbar and the brucite inclusion disappears (corresponding to the red line in Figures 5a and 5b). In contrast, for a periclase-inclusion with smaller fluid

pressure, the initially steep fluid pressure gradients are maintained during fluid pressure evolution, and the increase of the minimal fluid pressure inside the inclusion slows down significantly. The model with a periclase-inclusion and with sustained steep fluid pressure gradients involves the spatial propagation of a sharp fluid pressure front, or reaction front. Modeling the propagation of such sharp reaction front is numerically more challenging than the scenario with a brucite-inclusion exhibiting a simple fluid pressure diffusion. Therefore, for the following HMC models, we focus on the scenario with periclase-inclusions.

3.3. HMC Model

We consider the full HMC model to investigate the impact of solid deformation and mechanical heterogeneity on the evolution of p_f and ϕ, and on the reaction front evolution. We consider linear viscous deformation and perform five models with increasing deformation complexity (Figure 6). The models include a circular ($\Gamma_1 = 10$) or elliptical inclusion with a vertical radius two or three times larger than the horizontal radius, for which $\Gamma_1 = 10$. In the inclusions, the fluid pressure ($p_f = 6.5$ kbar) is initially smaller than the outside ambient pressure ($p_f = 8.5$ kbar). For all models, $\Gamma_2 = 10^8$ and $\Gamma_3 = 1$, except that η^s inside the inclusion is a factor 1,000 smaller than outside. We assume that the effective shear viscosity of the high-porosity, poroviscous periclase-water region is much smaller than the effective viscosity of the low-porosity brucite region and, hence, apply a smaller shear viscosity inside the inclusion. The first HMC model has a circular inclusion and no far-field deformation ($\Gamma_4 = 0$; Figure 6b), the second HMC model has a circular inclusion and far-field deformation ($\Gamma_4 = 0.0024$; Figure 6c), the third HMC model has an elliptical inclusion with aspect ratio of two and far-field deformation (result only shown in Figure 7), and the fourth HMC model has an elliptical inclusion with aspect ratio of three and far-field deformation ($\Gamma_4 = 0.0024$; Figure 6d). We apply relatively similar inclusion aspect ratios of two and three because for small aspect ratios the impact of the aspect ratio on the inclusion pressure is largest in purely mechanical models (e.g., Moulas et al., 2014, their Figure 8a; Luisier et al., 2019, their Figure 6b). For comparison with the HMC models, we also show the corresponding HC model, for which solid velocities are zero (Figure 6a).

In all models, the stability field of periclase, and the associated high-porosity region, is growing with time due to diffusion of p_f (e.g., Figure 6). In the HMC model without far-field deformation, the solid velocities indicate a radially symmetric contraction of the solid (Figure 6b). The direction of solid and fluid velocities is nearly identical. In the HMC model with circular inclusion and far-field pure-shear deformation, away from the circular inclusion, the solid velocities indicate the applied horizontal shortening and vertical extension (Figure 6c). Around the inclusion, the solid velocities change direction and show a radial contraction. Inside the inclusion, the directions of solid and fluid velocities are different. In the HMC model with far-field deformation and elliptical inclusion, the solid velocities indicate horizontal shortening and vertical extension, and around the inclusion contraction (Figure 6d). Inside the inclusion, the directions of solid and fluid velocities are different. For all HMC models, the maximal fluid velocities are approximately 7 orders of magnitudes larger than the solid velocities (see also Figures 9d and 9e). The order of magnitude of the fluid velocity can be estimated from Equation 6. Based on the applied parameters (Equation 15), assuming no solid velocity, a fluid-pressure gradient of 2 kbar/cm, and a representative porosity of 0.1 yields 2×10^{-8} m/s. For the HMC models with far-field deformation, the shortening velocity is the product of shortening rate and half-model width, which yields according to the values in Equation 15 a solid velocity of 10^{-15} m/s.

With progressive time, the horizontal profiles, centered vertically, of p_f and ϕ differ for the five models (Figures 7a and 7b). Profiles of p_f and ϕ are similar for the two HMC models with circular inclusion, indicating that far-field deformation does not significantly affect the evolution of p_f and ϕ. However, profiles of p_f and ϕ are different for the HMC models with elliptical inclusions and show a broader region with periclase and, hence, a more displaced dehydration front. The width of the periclase region in the HC model is similar to the width in the two HMC models with circular inclusions, whereas p_f has diffused slightly less for the two HMC models. The similar width of the periclase region for the HC and HMC models with circular inclusion shows that solid deformation has a minor impact on the propagation of the dehydration front for the applied configuration. The reason is that weak circular inclusions under far-field deformation do not generate a perturbation in p with respect to the far-field value of p (e.g., Moulas et al., 2014). This is different for weak elliptical inclusions with the long axis orthogonal to the shortening direction, as applied here, which

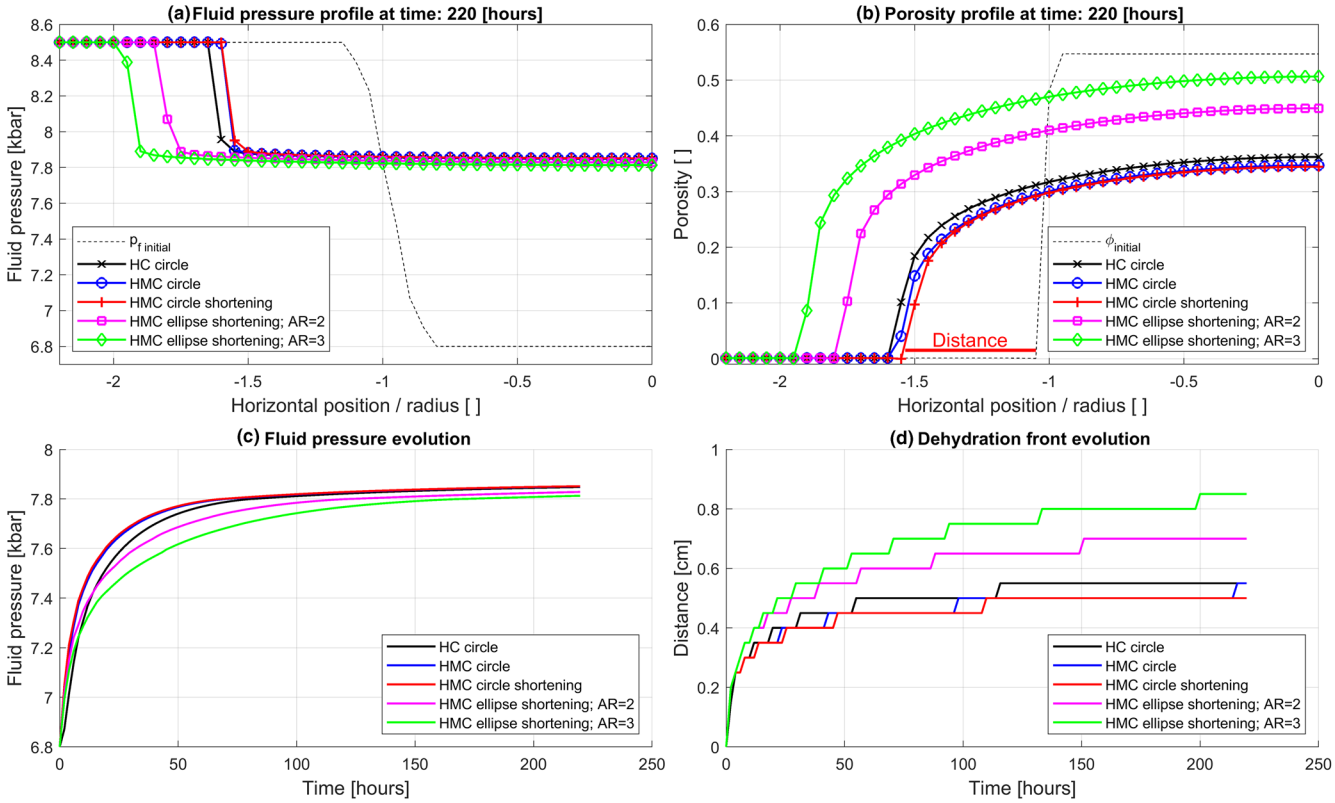

Figure 7. Horizontal profiles of fluid pressure and porosity for the models presented in Figure 6 and an additional model with elliptical inclusion having an initial aspect ratio of two. The profiles are centered vertically, corresponding to the bottom of the color plots displayed in Figure 6. (a) Profile of fluid pressure and (b) porosity for a modeled time of 220 h. (c) Time evolution of fluid pressure in the center of the inclusion corresponding to horizontal position 0 in (a). (d) Time evolution of the distance between the current location of the dehydration front and the initial location. This distance is indicated by the width of the horizontal red line in (b) for the HMC model with circular inclusion and shortening (red line). The lines in (d) show a stair-step pattern because the reaction front propagates in a discrete manner and, hence, the distance of the reaction front increases only by increments that are equal to the horizontal grid spacing.

exhibit higher p inside the inclusion compared to the far-field value (e.g., Moulas et al., 2014). For circular and elliptical inclusions, the distribution of p inside the inclusion is homogeneous (e.g., Moulas et al., 2014). The higher p inside elliptical inclusions causes a higher p_f, with respect to circular inclusions, and, hence, a wider diffusion region (Figure 7). Furthermore, values of p inside elliptical inclusions are larger for higher aspect ratios, which explains why the elliptical inclusion with an aspect ratio of 3 has a broader diffusion region than the inclusion with an aspect ratio of 2 (Figure 7).

With progressive time, p_f diffuses fastest for the two HMC models with circular inclusion and slowest for the HMC model with an elliptical inclusion of aspect ratio three (Figure 7c). For all models, diffusion of p_f is fastest during the initial stage of the simulations and progressively slows down significantly (Figure 7c). The diffusion of p_f controls the displacement of the dehydration front, which shows a similar nonlinear time evolution as p_f (Figure 7d). The dehydration front in the HMC model with elliptical inclusion of aspect ratio three moves fastest whereas the dehydration front for the HMC models with circular inclusion moves slowest. For the applied parameters, the dehydration front has moved a distance between $r/2$ (i.e., 0.5 cm) and r within 220 h (9.2 days). The results show that deformation of a mechanically heterogeneous medium has an impact on the evolution of fluid pressure and of the reaction front, which depends on the geometry of the heterogeneity. Additional figures showing more results of the five simulations presented in Figure 7 are available in the supplementary information (Figures S1–S5).

The model domain represents a deforming, heterogeneous rock in which a dehydration reaction occurs. The effective viscosity of the heterogeneous rock, $\overline{\eta}$, can be calculated by the ratio of $\langle \tau_{II} \rangle$ / $2\overline{D}_{xx}$, where $\langle \tau_{II} \rangle$ is the area-averaged value of τ_{II} and $\overline{D}_{xx}$ represents the second invariant of the deviatoric strain rate tensor

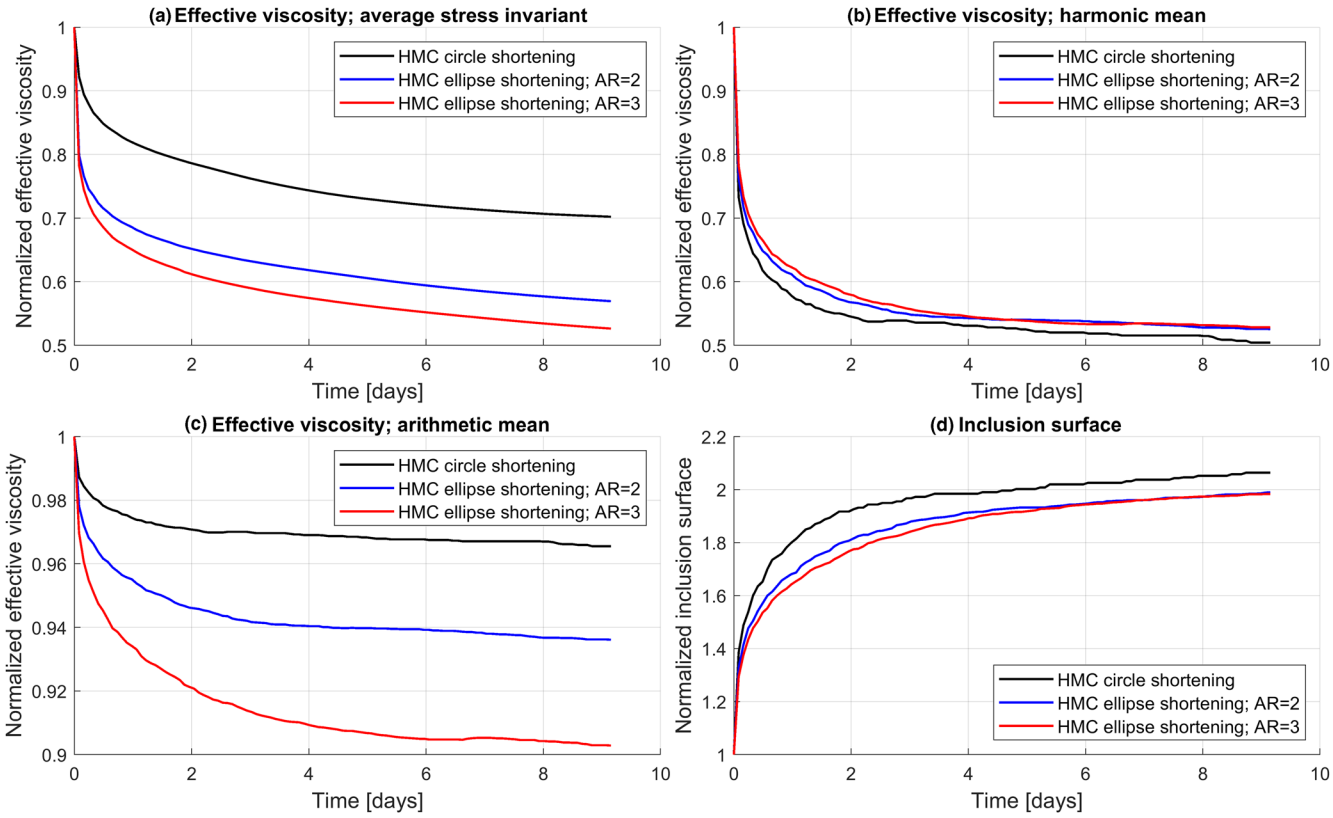

Figure 8. Reaction-induced weakening with progressive time is quantified by the decrease of the effective viscosity (a–c) of the entire model domain of three simulations presented in Figure 7 (see legends). (a) The effective viscosity is calculated by the area-average of the second invariant of the stress tensor divided by the second invariant of the far-field, pure-shear, strain rate invariant, which is constant throughout the simulation. (b) The effective viscosity is calculated by the harmonic mean of all viscosities at all numerical grid points. (c) Same as (b) but for arithmetic average. All effective viscosities are divided, normalized, by the initial effective viscosity of the first numerical time step. (d) Relative increase of the inclusion surface, divided by initial inclusion surface, with time.

corresponding to the applied bulk pure-shear deformation, which is constant throughout the simulations. The progressive dehydration reaction decreases the value of $\overline{\eta}$ with progressive deformation because the surface of the weak inclusion increases and the stress field changes (Figures 8a and 8d). The decrease of $\overline{\eta}$ with progressive reaction and deformation represents a reaction-induced weakening of the heterogeneous rock. The weakening is fastest at the beginning of deformation and subsequently slows down significantly. This overall weakening evolution is linked to the evolution of the inclusion surface (Figure 8d), which grows fastest at the beginning of the simulation and then subsequently slows down. However, the magnitude of the weakening, here between 30% and 50% effective viscosity reduction (Figure 8a), depends on the inclusion shape, and elliptical inclusions with larger aspect ratio exhibit more weakening (Figure 8a). For comparison, we also show the evolution of the harmonic average, or mean, and of the arithmetic average of the viscosity fields (Figures 8b and 8c). The simulations employ a linear shear viscosity and, therefore, the evolution of the harmonic and arithmetic mean of the viscosity field depends only on the relative inclusion surface inside the model domain. The results show a strongly nonlinear weakening with time and, hence, with progressive bulk strain since the applied bulk far-field pure-shear strain rate is constant.

To illustrate all features of our HMC model, we present results of a simulation with an oblique elliptical inclusion and a power-law viscous medium (Figures 9 and 10; the convergence test shown in Figure 3 was done for this simulation). The long axis of the elliptical inclusion forms a 60° angle with the horizontal shortening direction. The applied dimensionless parameters are $\Gamma_1 = 10$, $\Gamma_2 = 10^8$, $\Gamma_3 = 1$, $\Gamma_4 = 0.0024$, $\Gamma_5 = 0.024$, and $n = 3$. Results are made dimensional with the example values used in Equation 15. Magnitudes of p and p_f are significantly different both inside and outside the inclusion (Figures 9a and 9b). While p is homogeneous inside the inclusion and varies outside, p_f, in contrast, varies inside the inclusion but

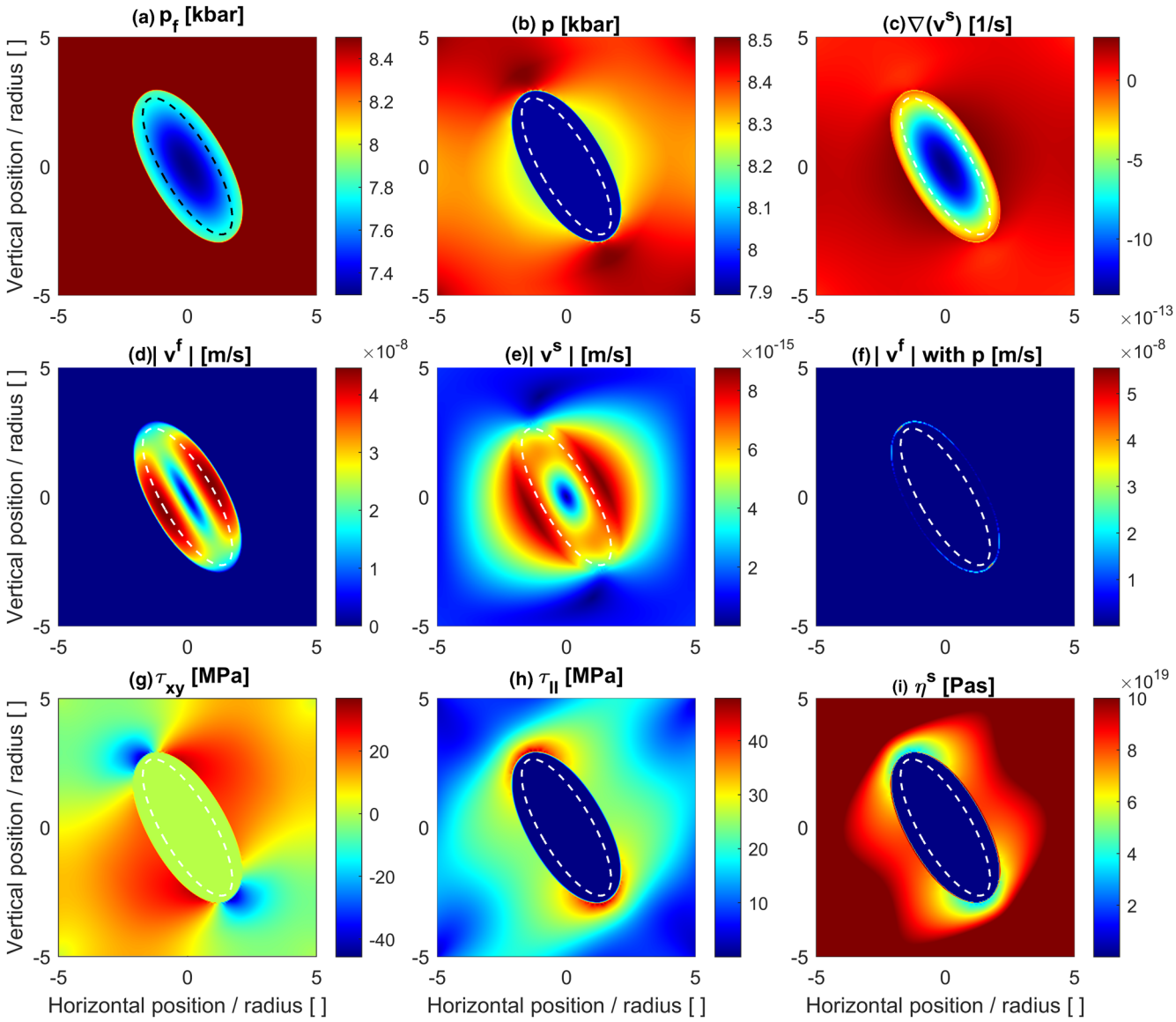

Figure 9. Color maps of model quantities (see Table 1) for an oblique elliptical inclusion with far-field horizontal pure shear shortening after a modeled time corresponding to 16.5 h. The material is power-law viscous with a stress exponent of 3, and the inclusion has a shear viscosity thousand times smaller than the surrounding. The physical units of the displayed quantities are given in the title of each panel. See text for more details.

is homogeneous outside. The divergence of the solid velocity, $\nabla\left(\mathbf{v}^s\right)$, shows contraction (negative values) inside the inclusion but mainly expansion (positive values) outside the inclusion (Figure 9c). The distribution of the absolute magnitude of the fluid velocity, $\left|\mathbf{v}^f\right| = \sqrt{\left(v_x^f\right)^2 + \left(v_y^f\right)^2}$, indicates that significant fluid flow only occurs inside the inclusion, where ϕ is large and where there is a gradient of p_f (Figure 9d). The absolute magnitude of the solid velocity, $\left|\mathbf{v}^s\right| = \sqrt{\left(v_x^s\right)^2 + \left(v_y^s\right)^2}$, shows that solid deformation is significant inside and outside the inclusion (Figure 9e). The magnitudes of absolute solid and fluid velocities indicate that fluid velocities, as estimated above, are approximately 7 orders of magnitude larger than the solid velocities. For illustration, we also calculate approximate fluid velocities by using p instead of p_f in the Darcy Equation 6. These approximate fluid velocities are zero inside the inclusion since p is homogeneous (Figure 9f). Hence, fluid velocities calculated with rock pressure gradients can be considerably different from the

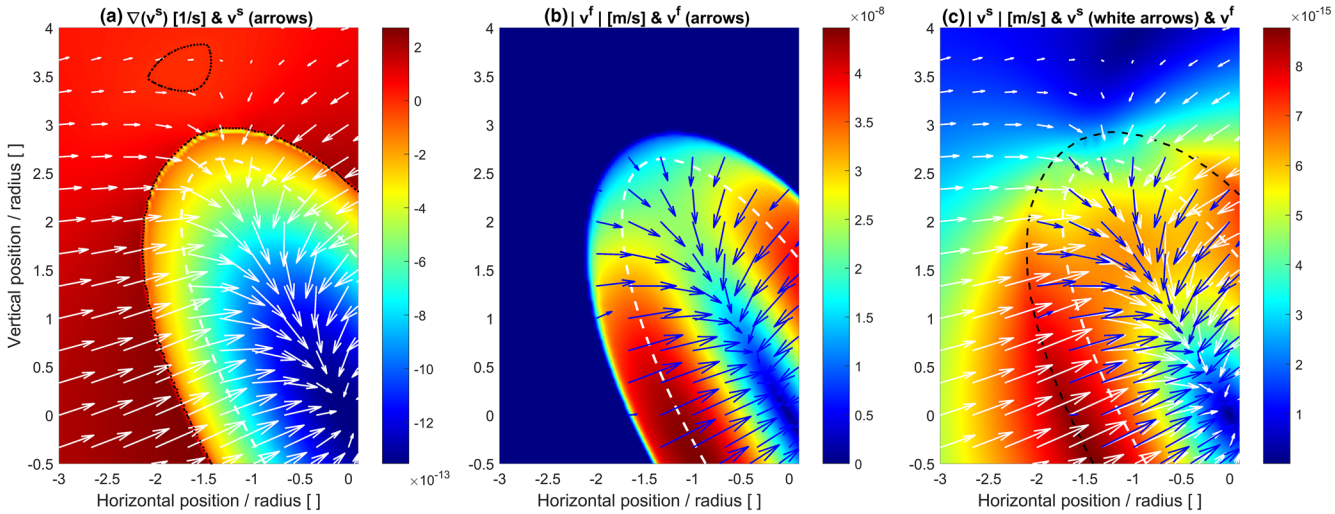

Figure 10. Enlargement of model results displayed in Figure 9. (a) Color plot of divergence of solid velocity field and arrows indicating solid velocity field. The dashed white line indicates the initial inclusion boundary and the black dotted line indicates the contour for which the divergence is zero. (b) Color plot of the absolute magnitude of fluid velocity and arrows indicating fluid velocity field. (c) Color plot of the absolute magnitude of solid velocity and arrows indicating solid and fluid velocity fields. Black dashed line indicates current reaction front. The physical units of the displayed quantities are given in the title of each panel.

fluid velocities calculated with fluid pressure gradients (Figures 9d and 9f). The shear stresses, τ_{xy}, inside the inclusion are significantly smaller than outside (Figure 9g), which is reasonable since the shear viscosity of the inclusion is 1,000 times smaller than the one of the surrounding. These shear stress variations also agree with analytical results for host-inclusion studies of Moulas et al. (2014). For the applied parameters, the largest magnitudes of τ_{xy} are in the order of 40 MPa. Also, τ_{II} is essentially homogeneous inside the inclusion and varies only outside (Figure 9h), which is the reason why the effective, stress-dependent shear viscosity of the solid, η^s, varies only outside the inclusion (Figure 9i). An enlargement of the model domain shows that the current inclusion boundary, representing the dehydration front, defines the transition from contraction inside the inclusion to expansion outside (Figure 10a). The applied far-field pure-shear, with horizontal shortening and vertical extension, would generate a zero divergence of the solid velocity, $\nabla \mathbf{v}^s$. Values of $\nabla \mathbf{v}^s$ are mostly positive outside the inclusion, indicating expansion, showing that the contraction inside the inclusion generates an expansion outside the inclusion to conserve total volume (Figure 10a), which is imposed by the volume conserving, pure-shear boundary conditions. For the presented results, we consider a pure-shear far-field shortening rate, $\bar{D}_{xx}$, of 2×10^{-14} s^{-1} (Equation 15). Maximal magnitudes of $\nabla \mathbf{v}^s$ are in the order of -1×10^{-12} s^{-1} showing that contraction rates are ~ 2 orders of magnitudes faster than the applied far-field shortening rates (Figure 10a). Fluid and solid velocities parallel to the short axis of the ellipse are significantly faster than the velocities parallel to the long axis (Figures 10b and 10c). Both magnitudes and directions of solid and fluid velocities are different inside the inclusion (Figures 10b and 10c). Furthermore, the direction of the reaction-front propagation is opposite to the direction of both solid and fluid velocities; while the solid and fluid velocities point toward the center of the inclusion, the reaction front moves away from the inclusion center (Figure 10c).

We run three additional simulations for the model configuration shown in Figure 9 keeping all parameters identical except: one simulation had an ambient porosity of 0.2 in the surrounding, and consequently a higher porosity in the inclusion; one simulation had a shear viscosity of the inclusion that was only a factor of 4 smaller than the one of the surrounding; and one simulation had a shear viscosity of the inclusion that was a factor of 4 larger than the one of the surroundings (i.e., a model with strong inclusion). The results are displayed in the supplementary information (Figures S6–S9). A comparison of the three additional simulations with the simulation displayed in Figure 9 shows: (1) A larger porosity generates larger values of both $\left|\mathbf{v}^s\right|$ and $\left|\mathbf{v}^f\right|$ (Figures S6 and S7). (2) A smaller viscosity ratio between surrounding and weak inclusion

generates larger values of τ_{xy} inside the inclusion, smaller values of $|\mathbf{v}^s|$, and larger variations of p and p_f between inclusion and surrounding (Figures S6 and S8). (3) A strong inclusion generates significantly smaller values of $|\mathbf{v}^s|$ but larger values of $|\mathbf{v}^f|$, higher τ_{xy} inside the inclusion and a larger variation of p between inclusion and surrounding (Figures S6 and S9).

4. Discussion

In the discretized PT mass conservation Equation 12, we keep the products of velocity, density, and porosity within the divergence term. We do not "open" the divergence term to obtain separate advection terms, for example, products of velocity multiplied by density gradient. Although we did not compare different numerical discretization schemes, we suggest that the applied conservative numerical scheme in fully divergent form is useful for numerical stability during modeling the propagation of sharp porosity and dehydration fronts, such as shown in Figures 5 and 7.

We consider a simple metamorphic reaction to investigate the fundamental impact of deformation in a heterogeneous solid on the reaction and fluid flow. It is, in principle, straightforward to extend the model to more complicated reactions involving more components, such as presented in Malvoisin et al. (2015). We assumed that the solid density is a function of the fluid pressure (Equation 8). Although for pure isotropic solids the density variations are a consequence of mean-stress variations (see Moulas et al., 2019, for discussion), it has been experimentally demonstrated that dehydration reactions are controlled by fluid pressure (e.g., Llana-Fúnez et al., 2012). When solid-fluid interactions are considered, the mean stress of the solid grains may not be the most appropriate macroscopic thermodynamic variable to quantify metamorphic phase equilibrium (e.g., Dahlen, 1992; see also discussion in Schmalholz & Podladchikov, 2014). For solid-fluid interactions, mineral devolatilization reactions must be investigated at the respective solid-fluid interface (e.g., Dahlen, 1992). However, our mathematical model constitutes a two-phase, or a superposed two-field, solid-fluid continuum, in which the solid-fluid interfaces are not resolved. Therefore, we need to approximate the thermodynamic pressure by some model quantity. For the (de)hydration reaction, the variation of total density is much larger than the density variation of the solid minerals. Therefore, the porosity evolution caused by the (de)hydration reactions controls the overall total density variation, and consequently, the volumetric deformation of the solid. Hence, we apply the fluid pressure as most appropriate proxy for the macroscopic thermodynamic pressure.

We model a closed system in equilibrium and assume that the transport of the hydrous fluid occurs by porous flow. Therefore, all the hydrous fluid required for the reaction is already in the system. Consequently, the reaction from periclase and H_2O-pure fluid to brucite decrease the volume of the system because the fluid in the pore space is bounded after the reaction in the brucite and porosity is significantly reduced. In an open system, the hydration of periclase, at pressure and temperature where brucite can form in the presence of water, generates a total-volume increase because water is added to the system during the reaction. Such hydration can cause reaction-induced fracturing in the rocks surrounding the hydrating periclase (e.g., Carmichael, 1987; Kuleci et al., 2017).

Our model configuration and results may be applicable to reactions related to fluid transfer inside and across shear zones. Moulas et al. (2014) showed that mathematical models of weak inclusions in viscous medium capture the first-order mechanical response of shear zones that develop in 2D visco-elasto-plastic thermo-mechanical numerical models during lithosphere shortening (e.g., Jaquet & Schmalholz, 2018; Schmalholz & Podladchikov, 2013). Fluid transfer and associated reactions are likely important during shear zone formation because the fluid enables reactions whose products can be weaker than the protolith (e.g., Jolivet et al., 2005). Therefore, fluid-driven mineral reactions can cause weakening during shear zone evolution, as was suggested for the fluid-controlled transformation from granulite to eclogite (e.g., Austrheim, 1987; Jamtveit et al., 2000; Jolivet et al., 2005). Due to the weakening, shear zones exhibit smaller effective viscosities and deviatoric stresses than the surrounding wall rock and can, hence, exhibit different fluid and solid pressures compared to the less-deforming wall rock (e.g., Jamtveit et al., 2018; Schmalholz & Podladchikov, 2013). Our model may be, hence, useful to study fluid transfer and reactions

in shear zones. Furthermore, our models show that reaction-induced weakening in a heterogeneous rock is strongly nonlinear with progressive time and, hence, progressive strain. Weakening is strongest during the initial stages of the reaction because it is controlled by fluid-pressure diffusion, which is controlled by the decreasing fluid pressure gradients. Also, significant reaction-induced weakening may occur within a small amount of strain because the fluid velocities, controlling reaction-front propagation, may typically be significantly faster than the solid velocities during tectonic deformation.

The applied model configurations with a single circular, or elliptical, inclusion were intentionally kept simple in order to investigate some fundamental features of coupling between heterogeneous deformation, fluid flow, and reactions, such as the propagation of a reaction front with steep gradients of fluid pressure and porosity. Potential future applications of our model could be the investigation of reaction-induced fracturing, for which elasticity should be considered in the constitutive equations and fracturing could be modeled, for example, by modeling brittle failure with a phase-field model, as was recently employed by Evans et al. (2020) to study hydration (serpentinization) of peridotite. Other potential applications could be to mechanically heterogeneous subduction interface shear zones with strong inclusions in a weak matrix, which we were recently studied numerically in the context of slow slip events and tremor (e.g., Beall et al., 2019a, 2019b; Webber et al., 2018). Our model could be useful to investigate the effects of fluid flow and reactions on slow slip events. Furthermore, the model could be elaborated to investigate the impact of (de) hydration reactions (e.g., serpentinitization or eclogitization), fluid flow, and reaction-induced weakening on the deformation dynamics along active subduction interfaces (e.g., Angiboust et al., 2012; Guillot et al., 2015). However, the computational performance of our algorithm must be improved to apply it to more natural shear zone geometries and to consider many inclusions, several reactions, and large strain. Such improvement could be made, for example, by translating the algorithm to the Julia programming language and utilizing parallel graphics processing unit computation (e.g., Besard et al., 2019).

5. Conclusions

The presented 2D HMC model and the applied PTFD numerical algorithm are suitable to quantify the interplay between metamorphic reactions and fluid flow in a deforming, heterogeneous, poroviscous medium. The medium is mechanically heterogeneous because the mineral-fluid assemblages involved in the reaction have different effective viscosities. Our model can simulate the power-law viscous deformation of a heterogeneous medium coupled to Darcy-type porous fluid flow, whereby solid and fluid velocities differ by 7 orders of magnitude. Furthermore, the model can simulate the propagation of a sharp, step-like, (de)hydration, porosity, and viscosity front.

Our results show that rock deformation and mechanical heterogeneities can have a considerable impact on fluid flow and metamorphic reactions because heterogeneities in deforming rock can cause rock pressure variations, which in turn cause fluid pressure variations that impact the reaction. In the simulations, the propagation of the reaction front during deformation causes a reaction-induced weakening of the heterogeneous rock because the surface of a weak mineral-fluid assemblage increases due to the reaction. This reaction-induced weakening is controlled by fluid-pressure diffusion and is strongly nonlinear with progressive strain, whereby weakening is most significant during the initial stages of the reaction. Also, in deforming heterogeneous rock, magnitudes, gradients, and distributions of fluid pressure and rock pressure can be significantly different so that also directions of fluid and solid velocities can be different. Therefore, models calculating fluid velocities from gradients of the rock pressure are likely considerably inaccurate if applied to deforming heterogeneous rock, such as in and around shear zones or plate boundary regions.

Data Availability Statement

All numerical results have been generated with a self-developed MATLAB algorithm, which is available on the platform Zenodo (https://doi.org/10.5281/zenodo.4051493) under: https://zenodo.org/badge/latestdoi/284908588

Acknowledgments
We are grateful to constructive comments and suggestions of J. Biemiller and an anonymous reviewer. This work was supported by the University of Lausanne. Evangelos Moulas acknowledges the Johannes Gutenberg University of Mainz for financial support. Oliver Plümper was supported by an ERC starting grant "nanoEARTH" (852069). Yuri Y. Podladchikov and Artem V. Myasnikov were supported by the Russian Ministry of Science and Higher Education (project no. 075-15-2019-1890).

References

Angiboust, S., Wolf, S., Burov, E., Agard, P., & Yamato, P. (2012). Effect of fluid circulation on subduction interface tectonic processes: Insights from thermo-mechanical numerical modelling. *Earth and Planetary Science Letters*, *357*, 238–248. https://doi.org/10.1016/j.epsl.2012.09.012

Austrheim, H. (1987). Eclogitization of lower crustal granulites by fluid migration through shear zones. *Earth and Planetary Science Letters*, *81*(2–3), 221–232.

Beall, A., Fagereng, A., & Ellis, S. (2019a). Fracture and weakening of jammed subduction shear zones, leading to the generation of slow slip events. *Geochemistry, Geophysics, Geosystems*, *20*, 4869–4884. https://doi.org/10.1029/2019GC008481

Beall, A., Fagereng, Å., & Ellis, S. (2019b). Strength of strained two-phase mixtures: Application to rapid creep and stress amplification in subduction zone Mélange. *Geophysical Research Letters*, *46*(1), 169–178. https://doi.org/10.1029/2018GL081252

Beinlich, A., John, T., Vrijmoed, J., Tominaga, M., Magna, T., & Podladchikov, Y. (2020). Instantaneous rock transformations in the deep crust driven by reactive fluid flow. *Nature Geoscience*, *13*(4), 307–311. https://doi.org/10.1038/s41561-020-0554-9

Besard, T., Foket, C., & De Sutter, B. (2019). Effective extensible programming: Unleashing Julia on GPUs. *IEEE Transactions on Parallel and Distributed Systems*, *30*(4), 827–841. https://doi.org/10.1109/TPDS.2018.2872064

Biot, M. A. (1941). General theory of three-dimensional consolidation. *Journal of Applied Physics*, *12*(February), 155–164.

Brantut, N., Stefanou, I., & Sulem, J. (2017). Dehydration-induced instabilities at intermediate depths in subduction zones. *Journal of Geophysical Research: Solid Earth*, *122*(8), 6087–6107. https://doi.org/10.1002/2017JB014357

Brantut, N., Sulem, J., & Schubnel, A. (2011). Effect of dehydration reactions on earthquake nucleation: Stable sliding, slow transients, and unstable slip. *Journal of Geophysical Research*, *116*(B5), B05304. https://doi.org/10.1029/2010JB007876

Carmichael, D. M. (1987), Induced stress and secondary mass transfer: Thermodynamic basis for the tendency toward constant-volume constraint in diffusion metasomatism. In H. C. Helgeson (Ed.), *Chemical transport in metasomatic processes. NATO ASI Series (Series C: Mathematical and Physical Sciences)* (pp. 239–264). Dordrecht: Springer.

Chorin, A. J. (1968). Numerical solution of the Navier-Stokes equations. *Mathematics of Computation*, *22*(104), 745–762.

Connolly, J. (1997). Devolatilization-generated fluid pressure and deformation-propagated fluid flow during prograde regional metamorphism. *Journal of Geophysical Research*, *102*(B8), 18149–18173.

Connolly, J. A. (2005). Computation of phase equilibria by linear programming: A tool for geodynamic modeling and its application to subduction zone decarbonation. *Earth and Planetary Science Letters*, *236*(1–2), 524–541. https://doi.org/10.1016/j.epsl.2005.04.033

Coussy, O. (2004). *Poromechanics*, Chichester, UK: John Wiley & Sons.

Dahlen, F. A. (1992). Metamorphism of nonhydrostatically stressed rocks. *American Journal of Science*, *292*(3), 184–198.

Duretz, T., Räss, L., Podladchikov, Y., & Schmalholz, S. (2019). Resolving thermomechanical coupling in two and three dimensions: Spontaneous strain localization owing to shear heating. *Geophysical Journal International*, *216*(1), 365–379. https://doi.org/10.1093/gji/ggy434

Escartin, J., Hirth, G., & Evans, B. (1997). Effects of serpentinization on the lithospheric strength and the style of normal faulting at slow-spreading ridges. *Earth and Planetary Science Letters*, *151*(3–4), 181–189.

Evans, O., Spiegelman, M., & Kelemen, P. B. (2018). A poroelastic model of serpentinization: Exploring the interplay between rheology, surface energy, reaction, and fluid flow. *Journal of Geophysical Research: Solid Earth*, *123*(10), 8653–8675. https://doi.org/10.1029/2017JB015214

Evans, O., Spiegelman, M., & Kelemen, P. B. (2020). Phase-field modeling of reaction-driven cracking: Determining conditions for extensive olivine serpentinization. *Journal of Geophysical Research: Solid Earth*, *125*(1), e2019JB018614. https://doi.org/10.1029/2019JB018614

Ferrand, T. P., Hilairet, N., Incel, S., Deldicque, D., Labrousse, L., Gasc, J., et al. (2017). Dehydration-driven stress transfer triggers intermediate-depth earthquakes. *Nature Communications*, *8*(1), 1–11. https://doi.org/10.1038/ncomms15247

Fletcher, R. C. (1974). Wavelength selection in the folding of a single layer with power-law rheology. *American Journal of Science*, *274*(11), 1029–1043.

Gerya, T. (2019). *Introduction to numerical geodynamic modelling*, Cambridge, UK: Cambridge University Press. https://doi.org/10.1017/9781316534243

Gerya, T. V., Connolly, J. A., & Yuen, D. A. (2008). Why is terrestrial subduction one-sided? *Geology*, *36*(1), 43–46. https://doi.org/10.1130/G24060A.1

Gomberg, J., Cascadia, & Group, B. W. (2010). Slow-slip phenomena in Cascadia from 2007 and beyond: A review. *Bulletin*, *122*(7–8), 963–978. https://doi.org/10.1130/B30287.1

Guillot, S., Schwartz, S., Reynard, B., Agard, P., & Prigent, C. (2015). Tectonic significance of serpentinites. *Tectonophysics*, *646*, 1–19. https://doi.org/10.1016/j.tecto.2015.01.020

Hobbs, B., & Ord, A. (2015), *Structural geology: The mechanics of deforming metamorphic rocks*. Amsterdam, The Netherlands: Elsevier. https://doi.org/10.1016/C2012-0-01215-X

Holland, T., & Powell, R. (1998). An internally consistent thermodynamic data set for phases of petrological interest. *Journal of Metamorphic Geology*, *16*(3), 309–343.

Jamtveit, B., Austrheim, H., & Malthe-Sørenssen, A. (2000). Accelerated hydration of the Earth's deep crust induced by stress perturbations. *Nature*, *408*(6808), 75–78.

Jamtveit, B., Moulas, E., Andersen, T. B., Austrheim, H., Corfu, F., Petley-Ragan, A., & Schmalholz, S. M. (2018). High pressure metamorphism caused by fluid induced weakening of deep continental crust. *Scientific Reports*, *8*(1), 17011. https://doi.org/10.1038/s41598-018-35200-1

Jamtveit, B., Petley-Ragan, A., Incel, S., Dunkel, K. G., Aupart, C., Austrheim, H., et al. (2019). The effects of earthquakes and fluids on the metamorphism of the lower continental crust. *Journal of Geophysical Research: Solid Earth*, *124*(8), 7725–7755. https://doi.org/10.1029/2018JB016461

Jaquet, Y., & Schmalholz, S. M. (2018). Spontaneous ductile crustal shear zone formation by thermal softening and related stress, temperature and strain rate evolution. *Tectonophysics*, *746*, 384–397. https://doi.org/10.1016/j.tecto.2017.01.012

John, T., Scambelluri, M., Frische, M., Barnes, J. D., & Bach, W. (2011). Dehydration of subducting serpentinite: Implications for halogen mobility in subduction zones and the deep halogen cycle. *Earth and Planetary Science Letters*, *308*(1–2), 65–76. https://doi.org/10.1016/j.epsl.2011.05.038

Jolivet, L., Raimbourg, H., Labrousse, L., Avigad, D., Leroy, Y., Austrheim, H., & Andersen, T. B. (2005). Softening trigerred by eclogitization, the first step toward exhumation during continental subduction. *Earth and Planetary Science Letters*, *237*(3–4), 532–547. https://doi.org/10.1016/j.epsl.2005.06.047

Kelemen, P. B., & Hirth, G. (2012). Reaction-driven cracking during retrograde metamorphism: Olivine hydration and carbonation. *Earth and Planetary Science Letters*, *345*, 81–89. https://doi.org/10.1016/j.epsl.2012.06.018

Kelemen, P. B., & Matter, J. (2008). In situ carbonation of peridotite for CO2 storage. *Proceedings of the National Academy of Sciences*, *105*(45), 17295–17300. https://doi.org/10.1073/pnas.0805794105

Kuleci, H., Ulven, O., Rybacki, E., Wunder, B., & Abart, R. (2017). Reaction-induced fracturing in a hot pressed calcite-periclase aggregate. *Journal of Structural Geology*, *94*, 116–135. https://doi.org/10.1016/j.jsg.2016.11.009

Lasaga, A. C. (1986). Metamorphic reaction rate laws and development of isograds. *Mineralogical Magazine*, *50*(357), 359–373.

Lindgren, W. (1912). The nature of replacement. *Economic Geology*, *7*(6), 521–535.

Llana-Fúnez, S., Wheeler, J., & Faulkner, D. R. (2012). Metamorphic reaction rate controlled by fluid pressure not confining pressure: Implications of dehydration experiments with gypsum. *Contributions to Mineralogy and Petrology*, *164*(1), 69–79. https://doi.org/10.1007/s00410-012-0726-8

Luisier, C., Baumgartner, L., Schmalholz, S. M., Siron, G., & Vennemann, T. (2019). Metamorphic pressure variation in a coherent Alpine nappe challenges lithostatic pressure paradigm. *Nature Communications*, *10*(1), 1–11. https://doi.org/10.1038/s41467-019-12727-z

Malvoisin, B., Austrheim, H., Hetényi, G., Reynes, J., Hermann, J., Baumgartner, L. P., & Podladchikov, Y. Y. (2020). Sustainable densification of the deep crust. *Geology*, *48*(7), 673–677. https://doi.org/10.1130/g47201.1

Malvoisin, B., Podladchikov, Y. Y., & Vrijmoed, J. C. (2015). Coupling changes in densities and porosity to fluid pressure variations in reactive porous fluid flow: Local thermodynamic equilibrium. *Geochemistry, Geophysics, Geosystems*, *16*(12), 4362–4387. https://doi.org/10.1002/2015GC006019

Moulas, E., Burg, J.-P., & Podladchikov, Y. (2014). Stress field associated with elliptical inclusions in a deforming matrix: Mathematical model and implications for tectonic overpressure in the lithosphere. *Tectonophysics*, *631*, 37–49. https://doi.org/10.1016/j.tecto.2014.05.004

Moulas, E., Schmalholz, S. M., Podladchikov, Y., Tajčmanová, L., Kostopoulos, D., & Baumgartner, L. (2019). Relation between mean stress, thermodynamic, and lithostatic pressure. *Journal of Metamorphic Geology*, *37*(1), 1–14. https://doi.org/10.1111/jmg.12446

Omlin, S., Malvoisin, B., & Podladchikov, Y. Y. (2017). Pore fluid extraction by reactive solitary waves in 3-D. *Geophysical Research Letters*, *44*(18), 9267–9275.

Philpotts, A. R., & Ague, J. J. (2009). *Principles of igneous and metamorphic petrology* (2nd ed., pp. 667). Cambridge, England: Cambridge University Press.

Plümper, O., John, T., Podladchikov, Y. Y., Vrijmoed, J. C., & Scambelluri, M. (2017). Fluid escape from subduction zones controlled by channel-forming reactive porosity. *Nature Geoscience*, *10*(2), 150–156. https://doi.org/10.1038/ngeo2865

Plümper, O., Røyne, A., Magrasó, A., & Jamtveit, B. (2012). The interface-scale mechanism of reaction-induced fracturing during serpentinization. *Geology*, *40*(12), 1103–1106. https://doi.org/10.1130/G33390.1

Poulet, T., Karrech, A., Regenauer-Lieb, K., Fisher, L., & Schaubs, P. (2012). Thermal–hydraulic–mechanical–chemical coupling with damage mechanics using ESCRIPTRT and ABAQUS. *Tectonophysics*, *526*, 124–132. https://doi.org/10.1016/j.tecto.2011.12.005

Putnis, A. (2009). Mineral replacement reactions. *Reviews in Mineralogy and Geochemistry*, *70*(1), 87–124. https://doi.org/10.2138/rmg.2009.70.3

Quinquis, M., & Buiter, S. (2014). Testing the effects of basic numerical implementations of water migration on models of subduction dynamics. *Solid Earth*, *5*(1), 537. https://doi.org/10.5194/se-5-537-2014

Räss, L., Duretz, T., & Podladchikov, Y. (2019). Resolving hydromechanical coupling in two and three dimensions: Spontaneous channelling of porous fluids owing to decompaction weakening. *Geophysical Journal International*, *218*(3), 1591–1616. https://doi.org/10.1093/gji/ggz239

Schmalholz, S. M., & Mancktelow, N. S. (2016). Folding and necking across the scales: A review of theoretical and experimental results and their applications. *Solid Earth*, *7*(5), 1417–1465. https://doi.org/10.5194/se-7-1417-2016

Schmalholz, S. M., Medvedev, S., Lechmann, S. M., & Podladchikov, Y. (2014). Relationship between tectonic overpressure, deviatoric stress, driving force, isostasy and gravitational potential energy. *Geophysical Journal International*, *197*(2), 680–696. https://doi.org/10.1093/gji/ggu040

Schmalholz, S. M., & Podladchikov, Y. Y. (2013). Tectonic overpressure in weak crustal-scale shear zones and implications for the exhumation of high-pressure rocks. *Geophysical Research Letters*, *40*(10), 1984–1988. https://doi.org/10.1002/grl.50417

Schmalholz, S. M., & Podladchikov, Y. (2014). Metamorphism under stress: The problem of relating minerals to depth. *Geology*, *42*(8), 733–734. https://doi.org/10.1130/focus0822014.1

Schmalholz, S. M., & Schmid, D. W. (2012). Folding in power-law viscous multi-layers. *Philosophical Transactions of the Royal Society A: Mathematical Physical and Engineering Sciences*, *370*(1965), 1798–1826. https://doi.org/10.1098/rsta.2011.0421

Schmid, D. W., & Podladchikov, Y. Y. (2003). Analytical solutions for deformable elliptical inclusions in general shear. *Geophysical Journal International*, *155*, 269–288. https://doi.org/10.1046/j.1365-246X.2003.02042.x

Schwartz, S. Y., & Rokosky, J. M. (2007). Slow slip events and seismic tremor at circum-Pacific subduction zones. *Reviews of Geophysics*, *45*(3). https://doi.org/10.1029/2006RG000208

Sulem, J., & Famin, V. (2009). Thermal decomposition of carbonates in fault zones: Slip-weakening and temperature-limiting effects. *Journal of Geophysical Research*, *114*(B3). https://doi.org/10.1029/2008JB006004

Webber, S., Ellis, S., & Fagereng, Å. (2018). "Virtual shear box" experiments of stress and slip cycling within a subduction interface mélange. *Earth and Planetary Science Letters*, *488*, 27–35. https://doi.org/10.1016/j.epsl.2018.01.035

Wheeler, J. (2018). The effects of stress on reactions in the Earth: Sometimes rather mean, usually normal, always important. *Journal of Metamorphic Geology*, *36*(4), 439–461. https://doi.org/10.1111/jmg.12299

White, S. t., & Knipe, R. (1978). Transformation-and reaction-enhanced ductility in rocks. *Journal of the Geological Society*, *135*(5), 513–516.

Yang, J., & Faccenda, M. (2020). Intraplate volcanism originating from upwelling hydrous mantle transition zone. *Nature*, *579*(7797), 88–91. https://doi.org/10.1038/s41586-020-2045-y

Yardley, B. W. (1989). *An introduction to metamorphic petrology*, Harlow, UK: Longman Scientific & Technical Harlow.

Yarushina, V. M., & Podladchikov, Y. Y. (2015). (De) compaction of porous viscoelastoplastic media: Model formulation. *Journal of Geophysical Research: Solid Earth*, *120*(6), 4146–4170. https://doi.org/10.1002/2014JB011258

Zheng, X., Cordonnier, B., Zhu, W., Renard, F., & Jamtveit, B. (2018). Effects of confinement on reaction-induced fracturing during hydration of periclase. *Geochemistry, Geophysics, Geosystems*, *19*(8), 2661–2672. https://doi.org/10.1029/2017GC007322